Scale- and Variable-Dependent Localization for 3DEnVar Data Assimilation in the Rapid Refresh Forecast System

Sho YOKOTA[1,2,3]**, Jacob R. CARLEY**[3]**, Ting LEI**[4,3]**, Shun LIU**[3]**, Daryl T. KLEIST**[3]**,**
Yongming WANG[5]**, and Xuguang WANG**[5]

[1]Numerical Prediction Development Center, Japan Meteorological Agency, Tsukuba, Ibaraki, Japan

[2]Meteorological Research Institute, Japan Meteorological Agency, Tsukuba, Ibaraki, Japan

[3]NOAA/NWS/NCEP/Environmental Modeling Center, College Park, Maryland, USA

[4]Lynker, College Park, Maryland, USA

[5]University of Oklahoma, Norman, Oklahoma, USA

Corresponding author: Sho Yokota (syokota@mri-jma.go.jp)

Key Points:

- This study implements scale- and variable-dependent localization (SDL and VDL) for data assimilation of the Rapid Refresh Forecast System.

- SDL decreases the imbalance of the analysis field and the bias of temperature and humidity forecasts by the larger localization radius.

- VDL enables simultaneous assimilation of conventional and radar reflectivity data without introducing noisy analysis increments.

Abstract

This study demonstrates the advantages of scale- and variable-dependent localization (SDL and VDL) on three-dimensional ensemble variational data assimilation of the hourly-updated high-resolution regional forecast system, the Rapid Refresh Forecast System (RRFS). SDL and VDL apply different localization radii for each spatial scale and variable, respectively, by extended control vectors. Single-observation assimilation tests and cycling experiments with RRFS indicated that SDL can enlarge the localization radius without increasing the sampling error caused by the small ensemble size and decreased associated imbalance of the analysis field, which was effective at decreasing the bias of temperature and humidity forecasts. Moreover, simultaneous assimilation of conventional and radar reflectivity data with VDL, where a smaller localization radius was applied only for hydrometeors and vertical wind, improved precipitation forecasts without introducing noisy analysis increments. Statistical verification showed that these impacts contributed to forecast error reduction, especially for low-level temperature and heavy precipitation.

1

Plain Language Summary

In atmospheric data assimilation based on ensemble forecasts, the analysis increment is limited to the vicinity of each observation by spatial localization to prevent spurious analysis increments due to sampling error caused by the small ensemble size. Scale- and variable-dependent localization (SDL and VDL) make it possible to set optimal localization radii separately for each spatial scale and variable. Sensitivity experiments in this study with a high-resolution forecast system showed that SDL could decrease the bias of temperature and humidity forecasts and that VDL could improve precipitation forecasts without introducing noisy analysis increments.

1. Introduction

To improve short-term high-resolution forecasts of severe weather, it is important to develop high-frequency ensemble-based atmospheric data assimilation (DA) methods (e.g., Dong and Xue 2013; Johnson and Wang 2017). Such methods utilize a high-resolution ensemble to estimate and evolve background error covariance (BEC), providing flow dependent covariances for the data assimilation algorithm. Two of the more common ensemble-based DA methods to assimilate high-resolution observations, such as radar data, are the ensemble Kalman filter (EnKF, Evensen 1994) and the ensemble-variational (EnVar, Hamill and Snyder 2000; Lorenc 2003).

In ensemble-based DA such as with EnKF and EnVar methods, the impact of assimilating observations is generally limited to the local vicinity of each observation utilizing spatial localization (Hamill et al. 2001; Houtekamer and Mitchell 2001). This spatial localization is required to mitigate the sampling error caused by the small ensemble sizes $\sim O(10^2)$. However, the small spatial localization limits the spatial extent of synoptic-scale analysis increments and introduces the dynamical imbalance of the analysis (e.g., Greybush et al. 2011).

To account for the disadvantage of small spatial localization, several multiscale localization methods were proposed. Zhang et al. (2009) suggested the successive covariance localization, which involves running the EnKF algorithm twice; the first pass uses a larger localization radius for so-called large-scale observations (e.g. rawinsondes) and a second pass uses a shorter

3

localization radius to assimilate dense convective-scale observations, such as those from Doppler radars [two-step DA (2DA) hereafter]. Miyoshi and Kondo (2013) suggested another two-step EnKF, which combines two independent EnKF analysis increments in the assimilation of the same observations with different localization radii. For EnVar, Buehner (2012) suggested a similar multiscale localization method, scale-dependent localization (SDL). SDL separates ensemble perturbations into multiple wavebands and different localization radii are simultaneously applied for each perturbation via extended control vectors. Buehner and Shlyaeva (2015) extended this SDL to include cross-scale BECs: this SDL has been tested with several operational global and regional EnVar systems (e.g., Caron and Buehner 2018, 2022; Caron et al. 2019; Huang et al. 2021). Although the simultaneous multiscale localization approach such as SDL is generally not applied in the EnKF with observation-space localization, it is also possible in an EnKF framework with model-space localization such as the multiscale local gain form ensemble transform Kalman filter (Wang et al. 2021).

The multiscale localization, such as SDL, attempts to mitigate sampling error without eliminating large-scale analysis increments by setting localization radii separately for synoptic- and convective-scales. However, the optimal localization radius also may depend on the control variables. In particular, the optimal localization radii of hydrometeors are smaller than other atmospheric variables, such as horizontal wind, temperature, and humidity (e.g., Michel et al. 2011). Furthermore, a smaller localization radius is generally optimal for variables associated

with dense spatial distributions, such as radar data (Perianez et al. 2014). These previous studies indicate the potential necessity of variable-dependent localization (VDL), which uses different localization radii for several variable groups. This facilitates the small-scale update of hydrometeors and the large-scale update of atmospheric variables simultaneously. Wang and Wang (2023, hereafter WW23) found large differences in correlation functions between hydrometeors and atmospheric variables at each decomposed scale. Therefore, they proposed and implemented SDL and VDL simultaneously in a regional EnVar system including radar DA and showed its advantage in a supercell case. Wang and Wang (2024) further applied this EnVar system to a CONUS case study of squall lines and demonstrated the benefits of SDL and VDL over the single-scale localization method in extracting information from the assimilated conventional in-situ and radar reflectivity observations.

As shown in WW23, SDL and VDL are beneficial in the regional EnVar framework, especially for radar DA. On the other hand, it has not been clear what kind of forecast indicators are statistically improved by application of SDL and VDL in an operational high-frequency DA system, or how much they are improved. This study implements SDL and VDL in the EnVar algorithm of the Rapid Refresh Forecast System (RRFS, Carley et al. 2023), which is the hourly-updated high-resolution (3 km grid spacing) regional forecast system being developed as the next operational regional forecast system for the National Weather Service. Further, we demonstrate which aspects of the forecast are improved when applying SDL and VDL by

5

109   examining impacts on near surface sensible weather, upper air forecast scores, and precipitation

110   via a series of sensitivity experiments. In particular, we focus on the impact of SDL and VDL

111   on decreasing the imbalance of the analysis.

112   The remainder of this paper is organized as follows. Section 2 explains the formulation of

113   SDL and VDL. Section 3 describes the experimental design of the SDL and VDL sensitivity

114   experiments. Section 4 describes the results of the experiments and discusses the impact of SDL

115   and VDL on the analysis and the forecast in the case of Hurricane Ian in 2022. Section 5 presents

116   the conclusions.

117

2. Formulation

118

a. Hybrid 3DEnVar

119

120   This study implements SDL and VDL in the Gridpoint Statistical Interpolation (GSI)-based

121   hybrid three-dimensional EnVar (3DEnVar) system (Wang et al. 2013). In this hybrid 3DEnVar,

122   the analysis increment $\delta\mathbf{x}$ is obtained by minimization of the cost function:

$$J(\delta\mathbf{x}_{st}, \mathbf{a}_1, \dots, \mathbf{a}_K) = \frac{1}{2}\beta_{st}(\delta\mathbf{x}_{st})^T \mathbf{B}_{st}^{-1}(\delta\mathbf{x}_{st}) + \frac{1}{2}\beta_{en}\sum_{k=1}^{K}(\mathbf{a}_k)^T \mathbf{L}^{-1}(\mathbf{a}_k) + \frac{1}{2}(\mathbf{H}\delta\mathbf{x} - \mathbf{d})^T \mathbf{R}^{-1}(\mathbf{H}\delta\mathbf{x} - \mathbf{d}), \qquad (1)$$

$$\delta\mathbf{x} = \delta\mathbf{x}_{st} + \sum_{k=1}^{K}\begin{bmatrix} \mathbf{a}_k \circ \mathbf{x}_k^{en(1)} \\ \vdots \\ \mathbf{a}_k \circ \mathbf{x}_k^{en(I)} \end{bmatrix}, \qquad (2)$$

123   where $\delta\mathbf{x}_{st}$ and $\mathbf{a}_k$ ($k = 1, \dots, K$; K is the ensemble size) are NI- and N-dimension

124   control vectors, respectively (N and I are the number of analysis grid points and the number

125   of variables, respectively), $\mathbf{B}_{st}$ in the first term of the right-hand side of Eq. (1) denotes the

126 static BEC ($NI \times NI$ matrix), $\mathbf{L}$ in the second term denotes the localization ($N \times N$ matrix),

127 and $\mathbf{R}$, $\mathbf{H}$, and $\mathbf{d}$ in the third term denote the observation error covariance ($M \times M$ matrix),

128 the linearized observation operator ($M \times NI$ matrix), and the M-dimension observation

129 innovation vector, respectively (M is the number of assimilated observations). β_{st} and β_{en}

130 ($1/\beta_{st} + 1/\beta_{en} = 1$) are the weights of the static and ensemble BECs, respectively. $\mathbf{x}_k^{en(i)}$ in

131 Eq. (2) is the N-dimension k-th ensemble perturbation vector (k-th ensemble member

132 subtracted by ensemble mean and normalized by $\sqrt{K-1}$) of the i-th kind of variable ($i =$

133 $1, \ldots, I$) and "∘" denotes the Schur product.

134

135 *b. Scale- and variable-dependent localization*

136 Earlier studies (Buehner and Shlyaeva 2015; Caron and Buehner 2018; Huang et al. 2021)

137 have implemented and explored SDL in the EnVar context. WW23 further proposed and

138 implemented both SDL and VDL within the GSI-based EnVar system. This subsection explains

139 how to implement SDL and VDL, mainly mirroring the notations of WW23. The scale

140 separation method for SDL realized by the recursive filter (Purser et al. 2003) is also shown

141 here.

142 In the formulation for SDL and VDL, the control vector $\mathbf{a}_k$ in Eq. (1) is extended to NSV-

143 dimension (S and V denote the total numbers of scales in SDL and variable groups in VDL,

144 respectively) as

$$\mathbf{a}_k = \begin{bmatrix} \begin{pmatrix} \mathbf{a}_{k,1,1} \\ \vdots \\ \mathbf{a}_{k,1,V} \end{pmatrix} \\ \vdots \\ \begin{pmatrix} \mathbf{a}_{k,S,1} \\ \vdots \\ \mathbf{a}_{k,S,V} \end{pmatrix} \end{bmatrix}, \tag{3}$$

145 and the analysis increment is written as

$$\delta \mathbf{x} = \delta \mathbf{x}_{st} + \sum_{k=1}^{K} \sum_{s=1}^{S} \begin{bmatrix} \mathbf{a}_{k,s,v(1)} \circ \mathbf{x}_{k,s}^{en(1)} \\ \vdots \\ \mathbf{a}_{k,s,v(I)} \circ \mathbf{x}_{k,s}^{en(I)} \end{bmatrix}, \tag{4}$$

146 where $v(i) \, [1 \le v(i) \le V]$ denotes the variable group number including the i-th variable.

147 Compared to Eq. (2), $\delta \mathbf{x}$ is created by the summation of each scale analysis increment and

148 $\mathbf{a}_{k,s,v(i)}$ is multiplied to the ensemble perturbations $\mathbf{x}_{k,s}^{en(i)}$ separately for each scale s and

149 variable group $v(i)$.

150 In this formulation, the localization $\mathbf{L}$ is also extended to $NSV \times NSV$ matrix as

$$\mathbf{L} = \begin{bmatrix} c_{1,1}^s \begin{pmatrix} c_{1,1}^v \mathbf{L}_{1,1}^{1/2} \mathbf{L}_{1,1}^{T/2} & \cdots & c_{1,V}^v \mathbf{L}_{1,1}^{1/2} \mathbf{L}_{1,V}^{T/2} \\ \vdots & \ddots & \vdots \\ c_{V,1}^v \mathbf{L}_{1,V}^{1/2} \mathbf{L}_{1,1}^{T/2} & \cdots & c_{V,V}^v \mathbf{L}_{1,V}^{1/2} \mathbf{L}_{1,V}^{T/2} \end{pmatrix} & \cdots & c_{1,S}^s \begin{pmatrix} c_{1,1}^v \mathbf{L}_{1,1}^{1/2} \mathbf{L}_{S,1}^{T/2} & \cdots & c_{1,V}^v \mathbf{L}_{1,1}^{1/2} \mathbf{L}_{S,V}^{T/2} \\ \vdots & \ddots & \vdots \\ c_{V,1}^v \mathbf{L}_{1,V}^{1/2} \mathbf{L}_{S,1}^{T/2} & \cdots & c_{V,V}^v \mathbf{L}_{1,V}^{1/2} \mathbf{L}_{S,V}^{T/2} \end{pmatrix} \\ \vdots & \ddots & \vdots \\ c_{S,1}^s \begin{pmatrix} c_{1,1}^v \mathbf{L}_{S,1}^{1/2} \mathbf{L}_{1,1}^{T/2} & \cdots & c_{1,V}^v \mathbf{L}_{S,1}^{1/2} \mathbf{L}_{1,V}^{T/2} \\ \vdots & \ddots & \vdots \\ c_{V,1}^v \mathbf{L}_{S,V}^{1/2} \mathbf{L}_{1,1}^{T/2} & \cdots & c_{V,V}^v \mathbf{L}_{S,V}^{1/2} \mathbf{L}_{1,V}^{T/2} \end{pmatrix} & \cdots & c_{S,S}^s \begin{pmatrix} c_{1,1}^v \mathbf{L}_{S,1}^{1/2} \mathbf{L}_{S,1}^{T/2} & \cdots & c_{1,V}^v \mathbf{L}_{S,1}^{1/2} \mathbf{L}_{S,V}^{T/2} \\ \vdots & \ddots & \vdots \\ c_{V,1}^v \mathbf{L}_{S,V}^{1/2} \mathbf{L}_{S,1}^{T/2} & \cdots & c_{V,V}^v \mathbf{L}_{S,V}^{1/2} \mathbf{L}_{S,V}^{T/2} \end{pmatrix} \end{bmatrix}, \tag{5}$$

151 where $\mathbf{L}_{s,v}^{1/2}$ denotes square root of the localization matrix $\mathbf{L}_{s,v}$ ($N \times N$ matrix) and is

152 realized by the recursive filter for the s-th scale in SDL and for the v-th variable group in VDL.

153 c_{s_1,s_2}^s ($s_1, s_2 = 1, \dots, S$) and c_{v_1,v_2}^v ($v_1, v_2 = 1, \dots, V$) are factors multiplying cross-scale and

154 cross-variable correlations, respectively. If $c_{s_1,s_2}^s = 1$ ("Cross" in Huang et al. 2021) and

155 $c_{v_1,v_2}^v = 1$ in all scales and variables, $\mathbf{L}$ is represented simply as

8

$$
\mathbf{L} = \begin{bmatrix} \begin{pmatrix} \mathbf{L}_{1,1}^{1/2} \\ \vdots \\ \mathbf{L}_{1,V}^{1/2} \end{pmatrix} \\ \vdots \\ \begin{pmatrix} \mathbf{L}_{S,1}^{1/2} \\ \vdots \\ \mathbf{L}_{S,V}^{1/2} \end{pmatrix} \end{bmatrix} \left[\left(\mathbf{L}_{1,1}^{T/2} \quad \cdots \quad \mathbf{L}_{1,V}^{T/2} \right) \quad \cdots \quad \left(\mathbf{L}_{S,1}^{T/2} \quad \cdots \quad \mathbf{L}_{S,V}^{T/2} \right) \right]. \tag{6}
$$

On contrary, if $c_{s_1,s_2}^s = \delta_{s_1 s_2}$ ("NoCross" in Huang et al. 2021) and $c_{v_1,v_2}^v = \delta_{v_1 v_2}$, all cross-scale and cross-variable correlations are ignored as

$$
\mathbf{L} = \begin{bmatrix} \begin{pmatrix} \mathbf{L}_{1,1}^{1/2} & & \mathbf{0} \\ & \ddots & \\ \mathbf{0} & & \mathbf{L}_{1,V}^{1/2} \end{pmatrix} & & \mathbf{0} \\ & \ddots & \\ \mathbf{0} & & \begin{pmatrix} \mathbf{L}_{S,1}^{1/2} & & \mathbf{0} \\ & \ddots & \\ \mathbf{0} & & \mathbf{L}_{S,V}^{1/2} \end{pmatrix} \end{bmatrix} \begin{bmatrix} \begin{pmatrix} \mathbf{L}_{1,1}^{T/2} & & \mathbf{0} \\ & \ddots & \\ \mathbf{0} & & \mathbf{L}_{1,V}^{T/2} \end{pmatrix} & & \mathbf{0} \\ & \ddots & \\ \mathbf{0} & & \begin{pmatrix} \mathbf{L}_{S,1}^{T/2} & & \mathbf{0} \\ & \ddots & \\ \mathbf{0} & & \mathbf{L}_{S,V}^{T/2} \end{pmatrix} \end{bmatrix}. \tag{7}
$$

In this study, the scale separation to obtain $\mathbf{x}_{k,s}^{en(i)}$ from the original ensemble perturbation

$\mathbf{x}_k^{en(i)}$ is achieved as

$$
\mathbf{x}_{k,s}^{en(i)} = \begin{cases} \mathbf{F}_{s,v(i)} \mathbf{x}_k^{en(i)} & (s = 1) \\ \mathbf{F}_{s,v(i)} \left[\mathbf{x}_k^{en(i)} - \mathbf{x}_{k,s-1}^{en(i)} \right] & (1 < s < S) \\ \mathbf{x}_k^{en(i)} - \mathbf{x}_{k,S-1}^{en(i)} & (s = S), \end{cases} \tag{8}
$$

where $\mathbf{F}_{s,v}$ is the low-pass filter realized by the recursive filter for the s-th scale in SDL and

the v-th variable group in VDL. The recursive filter in calculating $\mathbf{F}_{s,v}$ should be normalized

to make the spatially-integrated value one while that in calculating $\mathbf{L}_{s,v}$ is normalized to make

the peak value one. The resulting power spectra of $\mathbf{x}_{k,s}^{en(i)}$ are quasi-Gaussian in the wave space

(see Appendix A). The scale separation based on Eq. (8) obtains each scale in order from the

largest scale with the recursive filter, which is not strictly the same as the approach used in

WW23 applying the diffusion operator (strict Gaussian) in order from the smallest scale.

However, the resulting power spectra was almost the same (not shown) and the computational

168 expense of Eq. (8) is less than that of WW23 because the recursive filter with less computational

169 complexity is used instead of the diffusion operator.

170

3. Experimental design

172 In this study, we implemented SDL and VDL in hybrid 3DEnVar of a prototype RRFS

173 (Carley et al. 2023). First, we conducted the control experiment of single scale localization

174 (SSL) without radar reflectivity DA and compared it to the experiment with SDL. After that,

175 we additionally assimilated radar reflectivity in the experiment with VDL and compared it to

176 the control experiment. As a reference, the experiment with the early operational multiscale

177 approach, which runs 3DEnVar twice with different localization radii for large- and convective-

178 scale observations (2DA), was conducted. We also include comparisons with experiments using

179 both SDL and 2DA as well as with both SDL and VDL. These experiments will be explained

180 in more detail later in this section.

181 The RRFS is the high-resolution forecast system based on the limited area model capability

182 for the non-hydrostatic finite-volume cubed-sphere dynamical core (FV3LAM, Lin 2004;

183 Putman and Lin 2007; Black et al. 2021), which is being developed as the next-generation

184 operational regional forecast systems in National Centers for Environmental Prediction (NCEP)

185 and may replace several existing regional systems [e.g., the North American Mesoscale (NAM;

186 Janjic 2003; Janjic and Gall 2012) 3-km nests and High-Resolution Ensemble Forecast system

187   (HREF; Roberts et al. 2019, 2020)]. The horizontal grid interval of the FV3LAM is 3 km for

188   both deterministic and ensemble forecasts. The number of vertical layers is 65 and the lowest

189   level thickness and the top of the model are 8 m and 2 hPa, respectively. Although the

190   operational RRFS will cover a North American domain, this study applies it only for the

191   CONUS (contiguous United States) domain and the number of grid cells is 1820 x 1092

192   horizontally. Physics schemes used in the FV3LAM for this study are listed in Table 1.

193   The schematics of the procedure of the experiments for this study are shown in Fig. 1. Here,

194   hourly analysis-forecast cycles with GSI-based 3DEnVar and FV3LAM (initiated at 03 and 15

195   UTC) and 36-hour forecasts (from the 3DEnVar analysis at 12 and 00 UTC) were repeated

196   every 12 hours. The BEC in 3DEnVar was purely ensemble-based and created by 1-hour

197   FV3LAM ensemble forecasts from the 30-member serial ensemble square root filter (EnSRF;

198   Whitaker and Hamill 2002). Just after each hourly EnSRF analysis, the ensemble mean was

199   replaced with the 3DEnVar analysis (recentering in Fig. 1), and the ensemble spread was

200   inflated by the relaxation-to-prior spread method (RTPS; Whitaker and Hamill, 2012) with the

201   factor of 0.85. Only for the analyses at 03 and 15 UTC, the BEC was created using a 9-hour

202   global ensemble forecast subset from the 80-member local gain form ensemble transform

203   Kalman filter (LGETKF; Hunt et al. 2007; Lei et al. 2018) run as a part of the Global DA

204   System (GDAS) operated by NCEP. The initial conditions (ICs) were created by deterministic

205   forecasts in the Global Forecast System (GFS, horizontal grid interval ~ 13 km) in NCEP and

global ensemble forecasts in GDAS (horizontal grid interval ~ 26 km) under constraints of

operational availability. Namely, the first guesses of the 3DEnVar at 03 and 15 UTC were a

downscaling of GFS 3-hour deterministic forecasts, and the initial states of 30-member

ensemble forecasts at 03 and 15 UTC were a downscaling of GDAS 9-hour ensemble forecasts

(first 30 of 80 members). The GFS deterministic forecasts were also used for the lateral

boundary conditions (LBCs) of all FV3LAM forecasts in the experiments for this study,

meaning also that lateral boundary perturbations were not introduced for the ensemble.

To verify the impacts of SDL for synoptic-scale analysis and VDL for radar reflectivity DA,

five sensitivity experiments were conducted in this study along with the control simulation. The

control experiment (hereafter CNTL) assimilated a similar set of observations associated with

the Rapid Refresh (RAP; Benjamin et al. 2004, 2016) and High Resolution Rapid Refresh

(HRRR; Dowell et al. 2022), which includes observations from METAR, rawinsondes, aircraft,

and radial winds of Weather Surveillance Radar-1988 Doppler (WSR-88D; Crum and Alberty

1993, Liu et al. 2016), in both 3DEnVar and EnSRF. Satellite radiance data was not assimilated.

The localization radii are prescribed somewhat differently between their respective

implementations in EnSRF and 3DEnVar algorithms. The former defines the radii as the cutoff

scale of the Gaspari-Cohn localization function (Gaspari and Cohn 1999) while the latter uses

the Gaussian localization function ($e^{-20/3}$-folding scale). Therefore, the localization radii were

set to 300 km horizontally and 1.1 scale heights vertically, while the corresponding $e^{-1/2}$-

225 folding scale in 3DEnVar was 82.158 km horizontally and 0.30125 scale heights vertically.

226 After 3DEnVar only, the lowest-level and soil temperature and specific humidity were adjusted

227 by land-snow DA with satellite-based soil temperature and specific humidity data (Benjamin et

228 al. 2022), and hydrometeors were adjusted by non-variational cloud-hydrometeor assimilation

229 with radar reflectivity and lightning data (Benjamin et al. 2021).

230   The difference in the settings of the sensitivity experiments is summarized in Table 2.

231 Neither SDL nor VDL was applied in CNTL ($L = 1$ and $J = 1$). In the experiment with SDL

232 (hereafter EXPSDL), only the horizontal localization radii in 3DEnVar were different from

233 CNTL and set to 1200 and 300 km for larger and smaller-scale ensemble perturbations with 2-

234 scale SDL ($L = 2$ and $J = 1$) including cross-scale covariance ($c_{1,1}^{s} = c_{1,2}^{s} = c_{2,1}^{s} = c_{2,2}^{s} = 1$).

235 These 2 scales were separated by the horizontal recursive filter with 300-km $e^{-20/3}$-folding

236 scale as shown in Fig. 2. The other four experiments directly assimilated radar reflectivity with

237 the method of Wang and Wang (2017) only in 3DEnVar, where the non-variational cloud-

238 hydrometeor assimilation (Benjamin et al. 2021) done in CNTL and EXPSDL was limited to

239 just clearing out rain, snow, and graupel without radar reflectivity observations. Here, only 10

240 dBZ and larger reflectivity data interpolated to the analysis grids were assimilated directly, and

241 5 dBZ and less reflectivity data, thinned at every other horizontal and vertical grid point, were

242 also assimilated as 0 dBZ observations. The observation error standard deviation was set to 5

243 dBZ. In EXP2DA, radar reflectivity was assimilated in the second pass of 3DEnVar with the

13

244 smaller horizontal localization radius (15-km $e^{-20/3}$-folding scale) just after the other

245 observations were assimilated in the first 3DEnVar pass (2DA as in Zhang et al. 2009). In

246 EXPVDL, on the other hand, radar reflectivity was assimilated simultaneously with the other

247 observations in a single 3DEnVar instance using VDL ($L = 1$ and $J = 2$): the horizontal

248 localization radii were set to 300 km for the conventional analysis variables (i.e., horizontal

249 wind, temperature, specific humidity, and surface pressure), and 15 km for the other analysis

250 variables added for the radar reflectivity DA (i.e., vertical wind, reflectivity, and mixing ratios

251 of cloud water, cloud ice, rain, snow, and graupel). The cross-variable covariance between these

252 two variable groups was decreased by multiplying the factor 0.05 (=15/300) to prevent too large

253 impacts of radar reflectivity DA ($c_{1,1}^v = c_{2,2}^v = 1$ and $c_{1,2}^v = c_{2,1}^v = 0.05$, see Appendix B).

254 EXPSDL2DA was the same as EXP2DA except applying SDL ($L = 2$ and $J = 1$) only for the

255 first 3DEnVar like EXPSDL. EXPSDLVDL was the same as EXPVDL except applying SDL

256 for atmospheric variables in addition to VDL ($L = 2$ and $J = 2$). In all experiments, the other

257 settings including the vertical localization radius were the same as CNTL. In all applications of

258 the EnSRF, radar reflectivity was not assimilated and neither SDL nor VDL was used.

259   We set the experimental period of the analysis-forecast cycles from 03 UTC, May 11 to 12

260 UTC, May 19, 2021 and from 15 UTC, September 29 to 00 UTC, September 30, 2022. These

261 periods were chosen to examine the impact of SDL and VDL in cases of severe local storms

262 (the former period) and a tropical cyclone (the latter). In May 2021, 287 tornadoes, the largest

14

263   in 2021, were reported in the U.S. For the May 11–19 period, most tornadoes were generated

264   in the south-central U.S. The strongest tornado in this period was generated in Texas at 0011

265   UTC on May 18 and ranked as EF2 (NCEI 2023). In September 2022, Hurricane Ian produced

266   catastrophic storm surge, winds, and floods. Ian reached its peak intensity of 72.0 m s^{-1} (a

267   category 5 hurricane) at 1200 UTC, 28 September, and made landfall in southwestern Florida

268   with winds of 66.9 m s^{-1} at 1905 UTC, September 28, and in South Carolina with winds of 36.0

269   m s^{-1} at 1805 UTC, September 30 (Bucci et al. 2023).

270

Table 1. List of physics schemes used in FV3-LAM.

Physics schemes	Specification
Cloud microphysics	Thompson-Eidhammer Aerosol Aware Microphysics (Thompson and Eidhammer 2014)
Planetary boundary layer	Mellor-Yamada-Nakanishi-Niino Eddy Diffusivity/Mass Flux (MYNN-EDMF; Nakanishi and Niino 2009; Olson et al. 2019; Angevine et al. 2020)
Surface layer	Mellor-Yamada-Nakanishi-Niino surface layer (Olson et al. 2021)
Gravity wave	Small Scale Gravity Wave Drag (SSGWD; Tsiringakis et al. 2017) and Turbulent Orographic Form Drag (TOFD; Beljaars et al. 2004)
Land	Rapid Update Cycle Land Surface Model (RUC LSM; Smirnova et al. 1997, 2000, 2016)
Long and short-wave radiation	Rapid Radiative Transfer Model for Global Circulation Models (RRTMG; Mlawer 1997; Iacono et al. 2008)
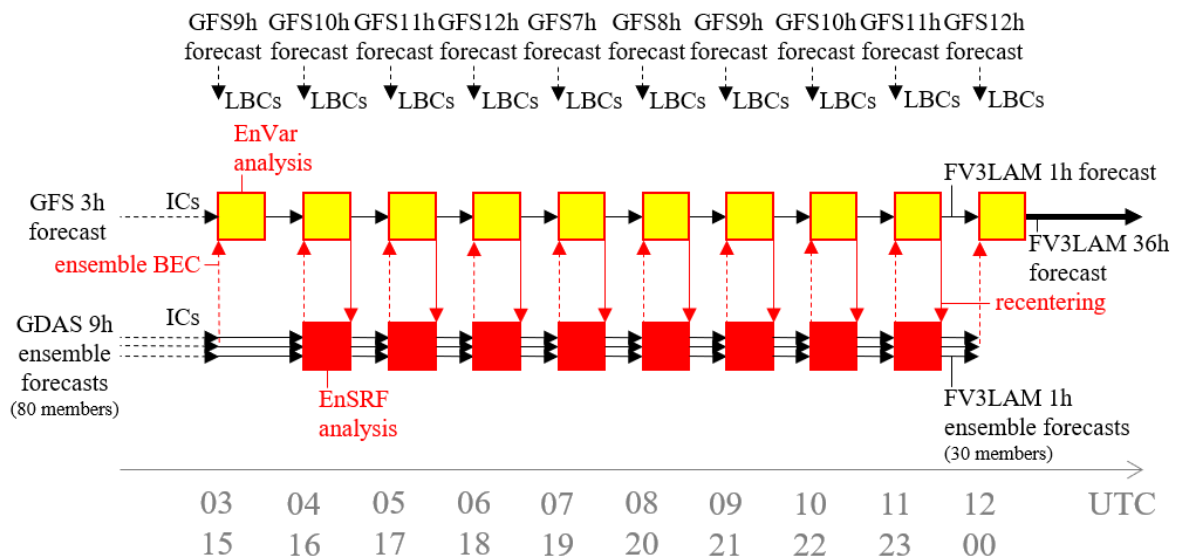
Fig. 1. Schematics of analysis-forecast cycling experiments.

Table 2. List of settings of EnVar in sensitivity experiments.

Name	Radar reflectivity DA	Horizontal localization radius ($e^{-20/3}$ scale)
CNTL	Not assimilated	300 km
EXPSDL	Not assimilated	1200 km (large-scale) 300 km (small-scale)
EXP2DA	Assimilated separately after conventional DA	300 km (conventional DA) 15 km (radar reflectivity DA)
EXPSDL2DA	Assimilated separately after conventional DA	1200 km (large-scale in conventional DA) 300 km (small-scale in conventional DA) 15 km (radar reflectivity DA)
EXPVDL	Assimilated simultaneously with conventional DA	300 km (atmosphere) 15 km (hydrometeors)
EXPSDLVDL	Assimilated simultaneously with conventional DA	1200 km (large-scale atmosphere) 300 km (small-scale atmosphere) 15 km (large-scale hydrometeors) 15 km (small-scale hydrometeors)
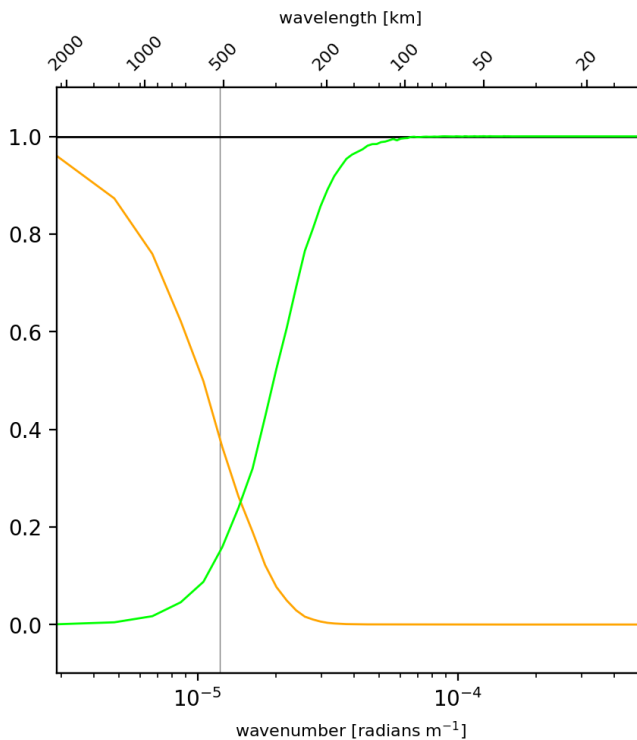
Fig. 2. The power spectrum density ratio of ensemble perturbations in SDL (black: original perturbation; orange: filtered perturbation by recursive filter; green: difference between original and filtered perturbations). Gray solid line indicates characteristic wavelength in scale separation (recursive filter $e^{-1/2}$-folding scale). Note that square roots of these two sum to one.

17

4. Results and discussion

a. Single observation experiments

In this subsection, we examine the impact of SDL and VDL first via a single observation experiment with pseudo surface pressure observation using the settings of CNTL, EXPSDL, and EXPVDL. We also include two additional experiments that are configured in the same manner as CNTL except use a single-scale horizontal localization radii ($e^{-20/3}$ scale) of 1200 km and 15 km (hereafter EXPSSL1200 and EXPSSL15, respectively). The horizontal localization function in each experiment is shown in Fig. 3. Each single observation experiment uses the same first guess field. The pseudo surface pressure observation having a first guess departure of –10 hPa and an observation error standard deviation of 1 hPa was assimilated in the northern region of Hurricane Ian at 80W and 31N at 16 UTC on September 29, 2022.

Figure 4 shows the analysis increments of the lowest-level temperature and sea level pressure (SLP) analysis in CNTL, EXPSSL1200, and EXPSDL. In CNTL, the analysis increments were limited within the northern part of the hurricane and the resulting surface pressure analysis was inconsistent with the expected axisymmetric hurricane structure (Fig. 4a). In EXPSSL1200, such unrealistic structure was not seen, and the hurricane was reasonably intensified because of the larger localization radius (Fig. 4b). However, the analysis increment was noisy north of the hurricane into South Carolina, likely due to sampling error. In EXPSDL (Fig. 4c), which includes both localization radii of CNTL and EXPSSL1200, the analysis

18

303　increments cover approximately the same area as EXPSSL1200 but are smoother overall.

304　Further, the analysis increment near the observation location remains similar to that noted in

305　the CNTL. The increments in the EXPSDL single observation experiment suggest that a large-

306　scale impact can be achieved in a way that reduces apparent sampling error.

307　　　The analysis increments of radar reflectivity at the lowest model level and SLP analysis for

308　CNTL, EXPSSL15, and EXPVDL are also shown in Fig. 5. In CNTL, the horizontal scale of

309　the analysis increment for radar reflectivity was as large as that for temperature (Figs. 4a and

310　5a) based on the localization function shown in the solid gray line in Fig. 3b. In EXPSSL15, on

311　the other hand, the smaller localization radius (dashed gray line in Fig. 3b) severely limits the

312　spatial extent of the analysis increment (Fig. 5b). Such small-scale analysis increments can

313　cause large dynamical imbalance of atmospheric variables. In EXPVDL with both localization

314　radii of CNTL (for horizontal wind, temperature, specific humidity, and surface pressure) and

315　EXPSSL15 (for vertical wind, reflectivity, and hydrometeors), the analysis of atmospheric

316　variables was identical to that in CNTL (compare SLP analyses in Figs. 5a and c). However,

317　the analysis increment of radar reflectivity in EXPVDL was smaller than that in CNTL and its

318　horizontal scale was between those in CNTL and EXPSSL15 (color in Fig. 5c) because the peak

319　value and the $e^{-20/3}$-folding scale of the localization function for cross-variable covariances

320　were approximately 0.005 and 212 km, respectively (see magenta line in Fig. 3b and Appendix

321　B).

19
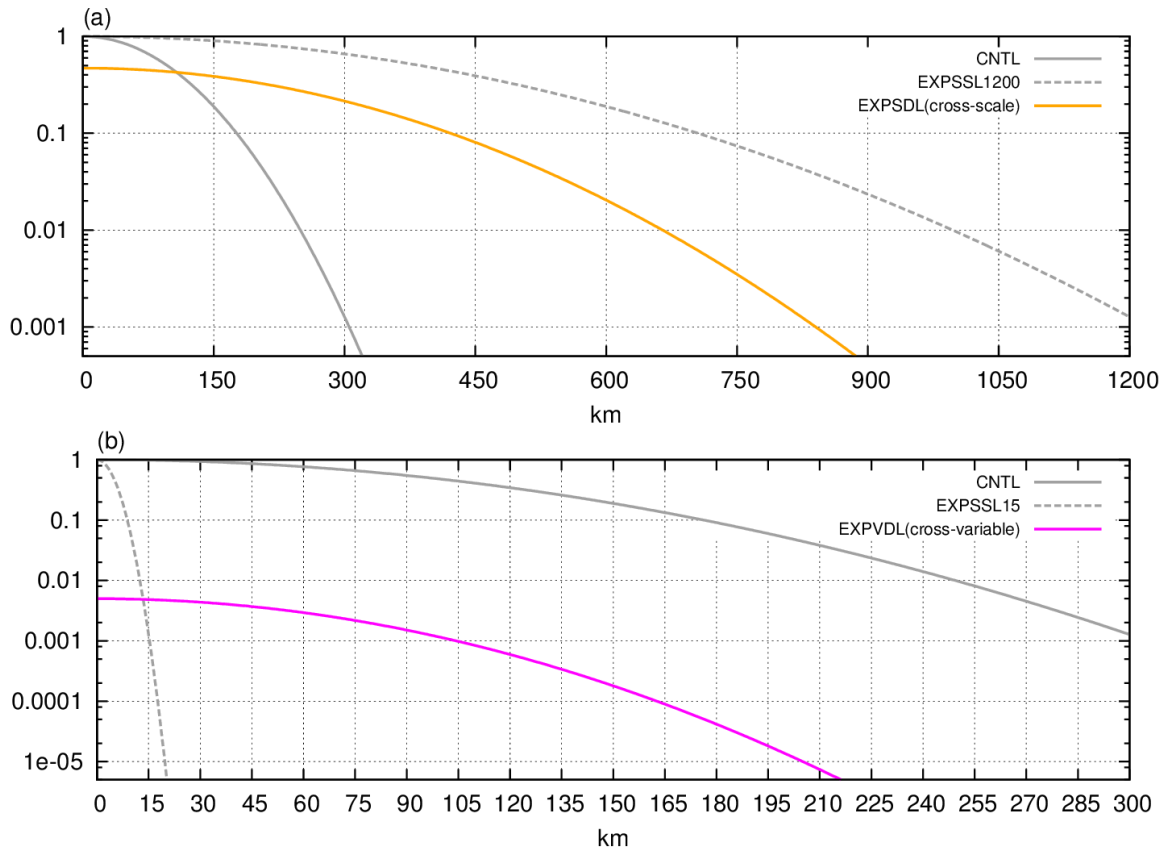
Fig. 3. Horizontal localization functions [a: CNTL (solid gray), EXPSSL1200 (dashed gray), and EXPSDL for the cross-scale covariance (orange); b: CNTL (solid gray), EXPSSL15 (dashed gray), and EXPVDL for the cross-variable covariance (magenta)]. Horizontal axis is the horizontal distance from the analysis point.
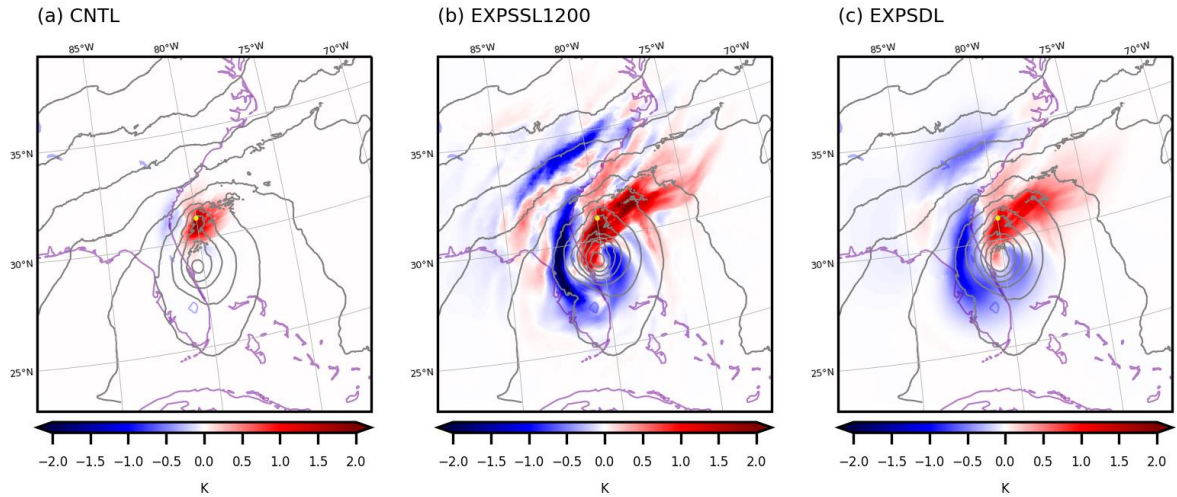
Fig. 4. Analysis increment of lowest-level temperature (color, K) and SLP analysis (gray contours, every 4 hPa) at 16 UTC on September 29, 2022 in the single surface pressure DA experiments (a: CNTL; b: EXPSSL1200; c: EXPSDL). Yellow dot is the position of the assimilated observation.
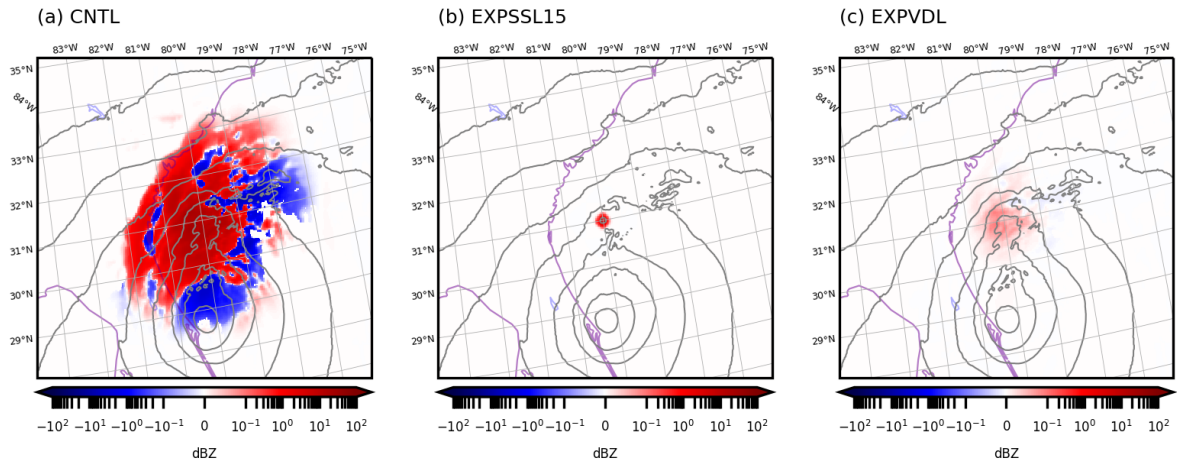
Fig. 5. Analysis increment of lowest-level radar reflectivity (color, dBZ) and SLP analysis (gray contours, every 4 hPa) at 16 UTC on September 29, 2022 in the single surface pressure DA experiments (a: CNTL; b: EXPSSL15; c: EXPVDL).

b. Statistical verification in cycling experiments

In this subsection, the impact of SDL and VDL is statistically verified in cycling experiments for May 11–19, 2021. For the verification of atmospheric variables, SDL had more impact than VDL as a whole. The relative impact of radar reflectivity DA to CNTL was almost the same between in two-step EnVar with 2DA (EXP2DA and EXPSDL2DA) and in simultaneous EnVar with VDL (EXPVDL and EXPSDLVDL).

Figure 6 shows the first guess departure of assimilated in-situ temperature, relative humidity, and horizontal wind observations. Compared to CNTL, the RMSE was significantly (confidence level $\geq 95\%$) smaller for temperature (Fig. 6a) and near-surface (> 950hPa) relative humidity (Fig. 6b) in the experiments with SDL (EXPSDL, EXPSDL2DA, and EXPSDLVDL). These RMSE reductions were associated with SDL making the horizontally averaged temperature warmer (Fig. 6d) and relative humidity dryer (Fig. 6e), respectively, in the corresponding vertical layers. The RMSE for low-level wind and its strong bias also tended to be smaller in the experiments with SDL (Figs. 6c and f). Note that SSL with a large localization length also decreased these biases, like SDL, but increased the RMSEs likely due to sampling error (Appendix C).

The impact of SDL shown above was also seen in the 12-hour upper-air forecast verified against radiosonde data for May 11–19, 2021 (Fig. 7): the cold bias of low-level (> 650hPa) temperature and the moist bias of low-level (> 850 hPa) relative humidity were clearly

22

decreased by SDL. These bias reductions were also clear in the surface verification. Both for

temperature (Fig. 8a) and for dew point temperature (Fig. 8b), the cold and moist biases were

decreased until the end of the forecast (36 hours). These SDL-induced bias reductions were

seen even with the radar reflectivity DA (compare EXPSDL2DA and EXPSDLVDL to

EXP2DA and EXPVDL, respectively, in Figs. 6–8). The cause of these bias reductions is

discussed in the next section. As for the near surface wind, the impact was neutral (not shown).

The radar reflectivity DA slightly increased and decreased the cold bias of low-level and

mid-level temperature, respectively (see the differences between the experiments with

(EXP2DA, EXPSDL2DA, EXPVDL, and EXPSDLVDL) and without (CNTL and EXPSDL)

radar reflectivity DA in Fig. 6d), and their associated RMSEs (Fig. 6a); this impact was

associated with increasing near-surface evaporation cooling and midlevel condensation heating.

In fact, near-surface and midlevel first guesses of temperature were clearly lower and higher,

respectively, in the precipitation region in EXP2DA and EXPVDL than those in CNTL (Fig. 9).

Please note that the impact of the radar reflectivity DA was smaller and only seen in the shorter-

range forecast than that of SDL (Figs. 6–8) since it was limited to the precipitation region.

As for radar reflectivity forecasts, the impacts of both SDL and VDL were clear. Figure 10

shows critical success index (CSI) and bias of 3-hour and 12-hour composite reflectivity

forecasts verified against the Multi-Radar Multi-Sensor (MRMS, Smith et al. 2016). It indicates

that radar reflectivity DA made both CSI and positive bias larger especially in the short-term

23

377 forecasts of low reflectivity. This impact was statistically significant and larger in EXP2DA

378 than in EXPVDL (Fig. 10a) and also seen in 12-hour forecasts except for the high reflectivity

379 (Fig. 10b). This positive bias of reflectivity forecasts was decreased by both SDL and VDL.

380 This SDL-induced bias reduction was larger than its increase by radar reflectivity DA in 12-

381 hour forecasts (Fig. 10b), and retained until the end of (36-hour) forecasts (not shown).

382 Although SDL did not significantly improve CSI in the 3-hour forecasts (Fig. 10a), it was

383 clearly improved by SDL especially in 12-hour forecasts for high reflectivity (Fig. 10b).

384
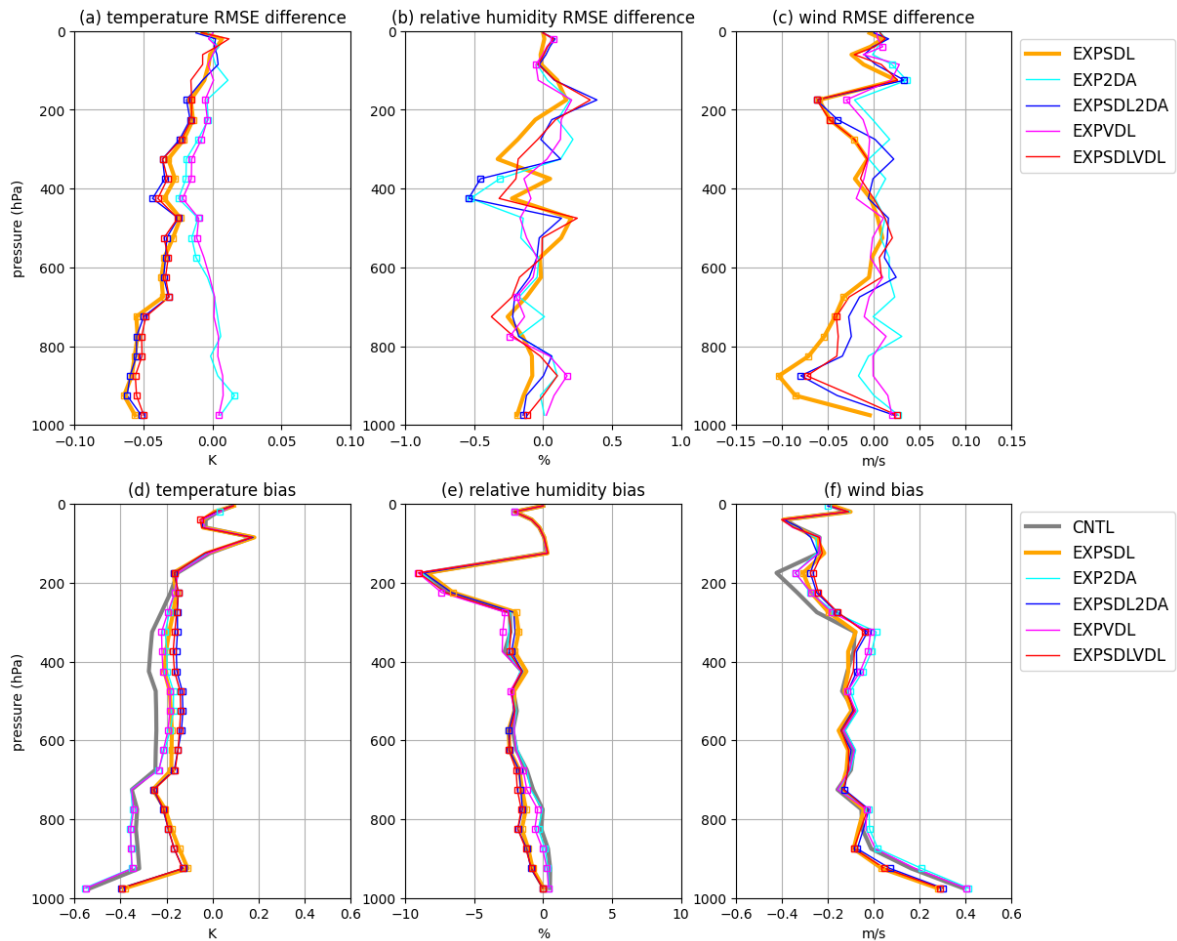
Fig. 6. Vertical profiles of first guess departure (a–c) standard deviations (difference from CNTL) and (d–f) biases verified against assimilated in-situ observations [a and d: temperature (K); b and e: relative humidity (%); c and f: horizontal wind (m s^{-1})] in each cycling experiment for May 11–19, 2021 (gray: CNTL; orange: EXPSDL; cyan: EXP2DA; blue: EXPSDL2DA; magenta: EXPVDL; red: EXPSDLVDL). Square marks indicate significantly different from CNTL (confidence level ≥ 95% in the t-test).
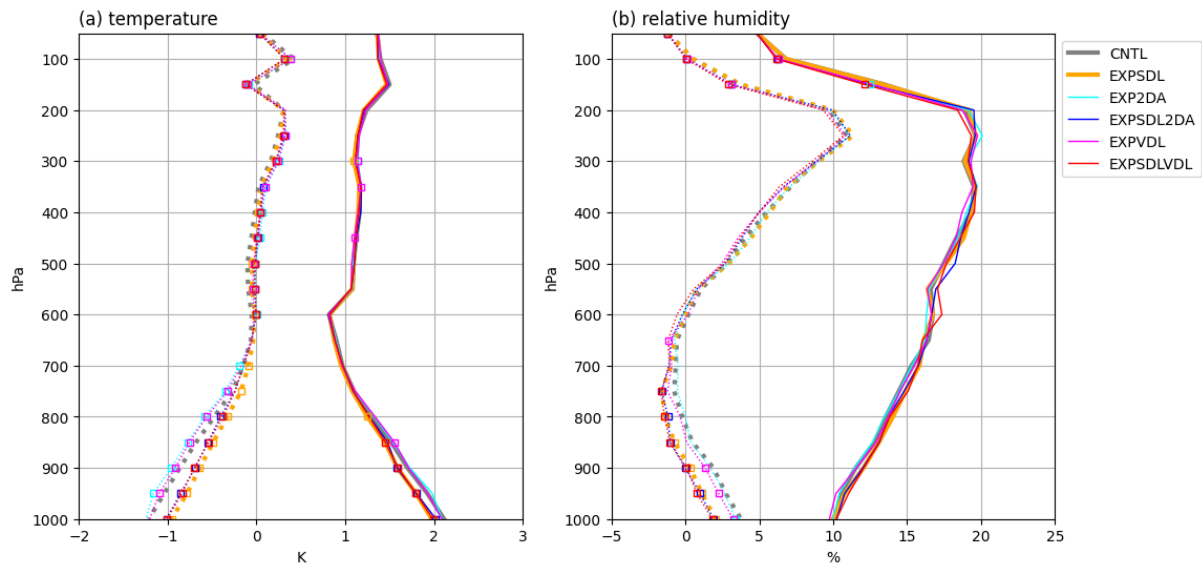
Fig. 7. Vertical profiles of 12-hour forecast RMSE (solid lines) and bias (dotted lines) verified against radiosonde (a) temperature (K) and (b) relative humidity (%) observations in each cycling experiment for May 11–19, 2021 (gray: CNTL; orange: EXPSDL; cyan: EXP2DA; blue: EXPSDL2DA; magenta: EXPVDL; red: EXPSDLVDL). The relative humidity forecast was computed with observed temperature. Square marks indicate significantly different from CNTL (confidence level ≥ 95% in the t-test).

401
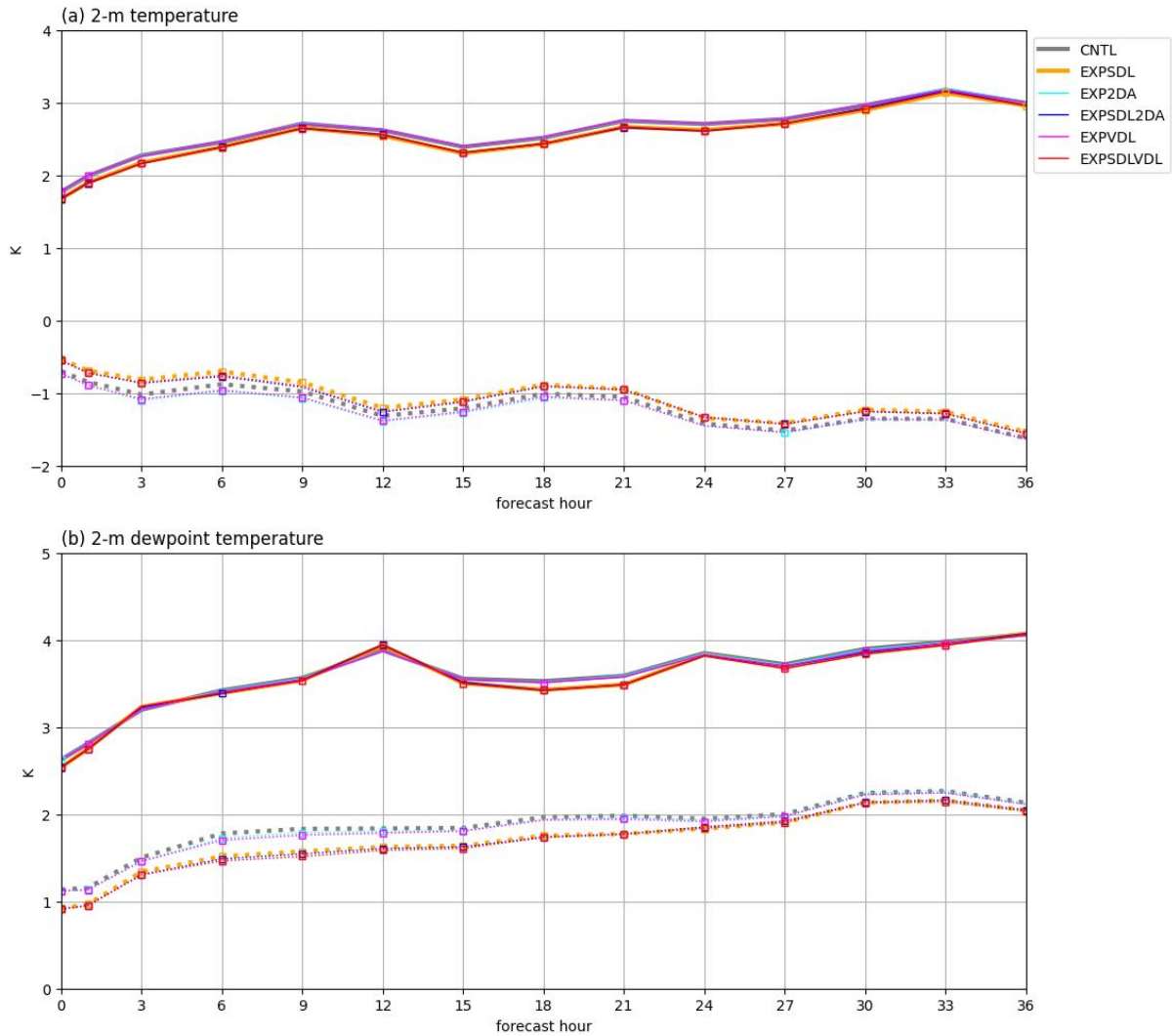
Fig. 8. Forecast RMSE (solid lines) and bias (dotted lines) verified against (a) temperature (K) and (b) dew point temperature (K) observations at 2-m AGL in each cycling experiment for May 11–19, 2021 (gray: CNTL; orange: EXPSDL; cyan: EXP2DA; blue: EXPSDL2DA; magenta: EXPVDL; red: EXPSDLVDL). Square marks indicate significantly different from CNTL (confidence level $\geq$ 95% in the t-test).

407
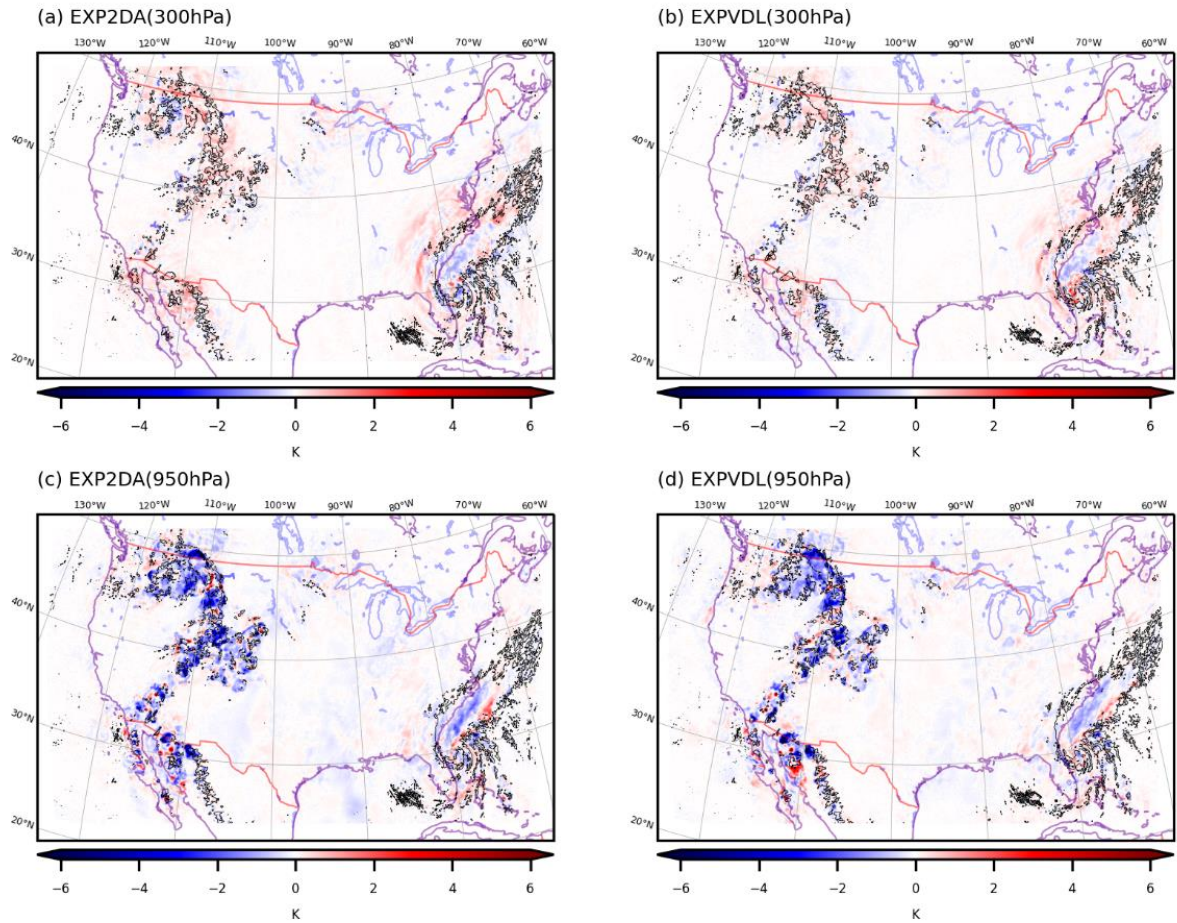
Fig. 9. Difference of 1-hour temperature forecasts in (a,b) 300 hPa and (c,d) 950 hPa at 00UTC, September 30, 2022 (a,c; EXP2DA-CNTL; b,d: EXPVDL-CNTL). Black contours are composited radar reflectivity forecasts (10 dBZ) in (a,c) EXP2DA and (b,d) EXPVDL.
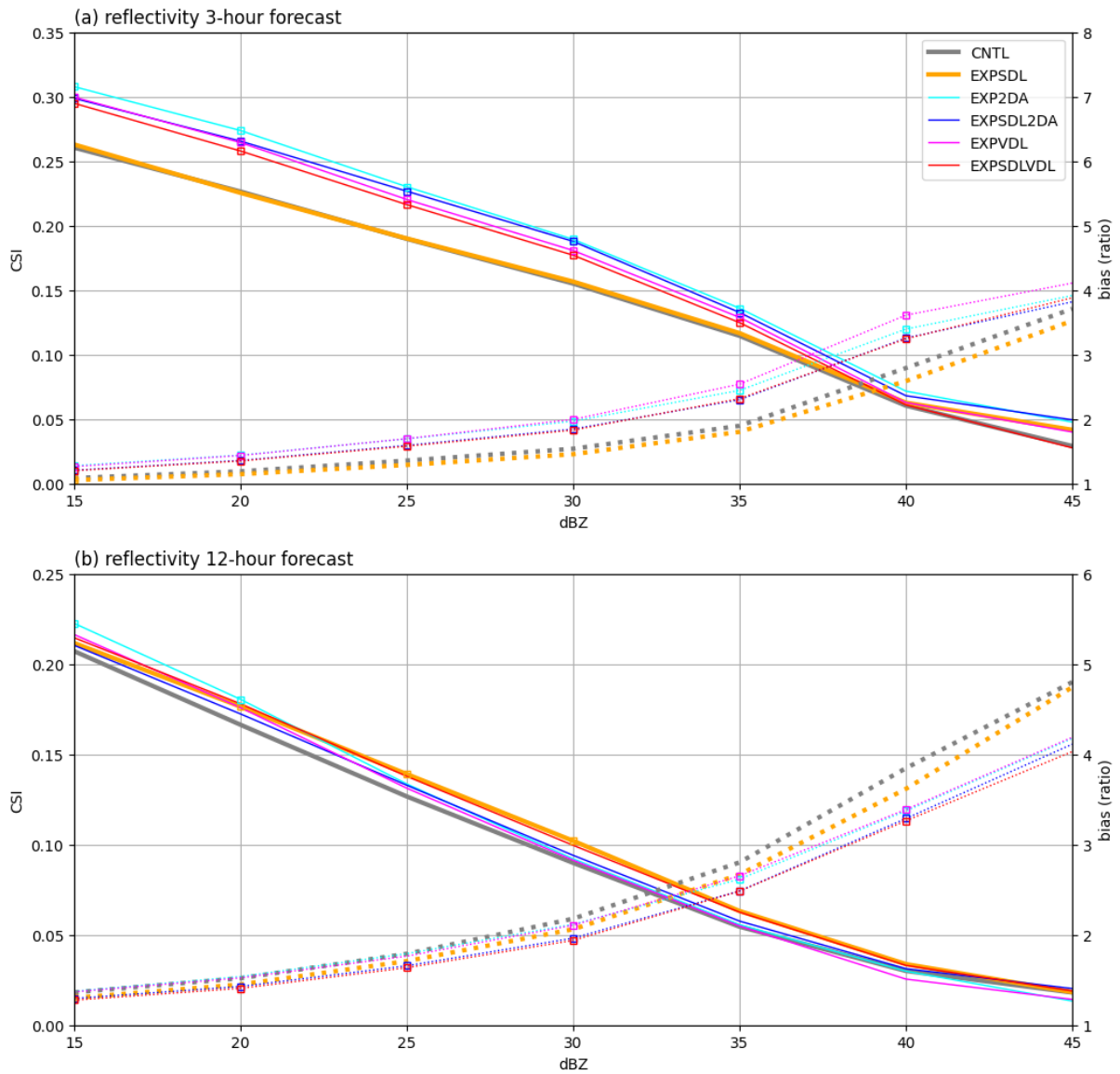
Fig. 10. CSI (solid lines) and bias (dotted lines) of (a) 3-hour and (b) 12-hour radar reflectivity forecasts verified against the MRMS composite reflectivity (thresholds: 15, 20, 25, 30, 35, 40, and 45 dBZ) in each cycling experiment for May 11–19, 2021 (gray: CNTL; orange: EXPSDL; cyan: EXP2DA; blue: EXPSDL2DA; magenta: EXPVDL; red: EXPSDLVDL). Square marks indicate significantly different from CNTL (confidence level ≥ 95% in the t-test).

c. Impacts on the hurricane analysis and forecast

In this section, the impacts of SDL and VDL shown in the previous section are discussed in more detail based on the case of Hurricane Ian in September 2022. The cold bias of low-level temperature seen in the period for May 11–19, 2021 was similarly decreased by SDL also in the period for September 29–30, 2022 (not shown).

Figure 11 depicts the analysis increments of surface pressure in each experiment at 16 UTC, September 29. In the experiments with SDL (Figs. 11b, d, and f), the analysis increment was horizontally smoother than those without SDL (Figs. 11a, c, and e) because the larger localization radius was applied for the larger-scale (smoothed) ensemble covariances in SDL. As a result, SDL reduced the horizontally-averaged first guess departure more than the experiments without SDL, which is why the bias of temperature and humidity was smaller in the experiments with SDL for the May cycling period of experiments (Figs. 6–8).

The relative smoothness of the analysis increment is dependent on the power spectra of the ensemble perturbations. For example, SDL also made the analysis increment of lowest-level temperature smoother horizontally (not shown). However, it was not as smooth as surface pressure because the power spectrum of large wavelength of lowest-level temperature was not larger relatively than that of surface pressure. Figure 12 shows the power spectra of one-member's ensemble perturbations of surface pressure and temperature used for ensemble-based BEC in the EnVar analysis at 16 UTC, September 29, which indicates the contribution ratio of

30

power spectrum of larger wavelength to the whole was larger in surface pressure (Fig. 12a) than that in lowest-level temperature (Fig. 12b). These power spectra in the logarithmic graph (Fig. 12) were nearly straight, even in the range of wavelengths of just several kilometers, which implies that the spin-up was completed in 1-hour forecasts in this case. Note that the power spectrum density ratio of ensemble perturbations separated by SDL (Fig. 2) did not depend on variables.

The smoother analysis increment caused by SDL does not necessarily decrease RMSE of the short-term forecast because the resulting analysis is not as close to the assimilated observations in the finer scale. However, it may be beneficial for the long-term forecast due to the smaller dynamical imbalance of the analysis. In fact, the mean surface pressure tendencies of the forecasts from the analyses at 00 UTC, September 30 were smaller in the experiments with SDL (Fig. 13).

Figure 13 also shows that radar reflectivity DA enlarged the imbalance. This tendency was seen especially in the experiments with 2DA (EXP2DA and EXPSDL2DA) because the smaller horizontal localization in the second pass of 3DEnVar limited the analysis increments of atmospheric variables only near assimilated observations (dashed gray line in Fig. 3b) and made them noisy (northeast coast of Florida in Figs. 11c and d). In the experiments with VDL (EXPVDL and EXPSDLVDL), the analysis increment was less noisy even with radar reflectivity DA than that in the experiments with 2DA (Figs. 11e and f) because the localization

31

458   function for cross-variable covariance between atmospheric and hydrometeor variables was

459   smaller and wider (magenta line in Fig. 3b). As a result, VDL kept the imbalance smaller even

460   while assimilating radar reflectivity and the imbalance reduction by SDL was clearer than the

461   experiments with 2DA.

462   The imbalance reduction by SDL and VDL also affected the track forecast of Hurricane Ian

463   (Figs. 14 and 15). In the experiments with radar reflectivity DA (Figs. 14c–f), the composite

464   reflectivity analyses were closer to the MRMS observation than that in CNTL near the center

465   of Ian. However, the analyses of SLP were less axisymmetric, and the resulting track forecast

466   had larger cross-track error in the experiments with 2DA (Figs. 14c and d) than those in the

467   other experiments (Fig. 15a). In the experiments with VDL (Figs. 14e and f), the cross-track

468   errors were as small as that in CNTL, and the composite reflectivity analyses were similar to

469   the experiments with 2DA. On the other hand, the intensification forecast of Ian (Fig. 15c) was

470   a little overestimated in EXPVDL probably because the smaller imbalance was more suitable

471   for the hurricane intensification than EXP2DA. This overestimation was not seen in comparison

472   between EXPSDLVDL and EXPSDL2DA. The larger-scale, smoother analysis increment in

473   EXPSDLVDL might affect the intensification forecast. Note that these impacts were seen in the

474   specific forecast, and SDL and VDL do not necessarily improve the track and intensification

475   forecasts. More cases would need to be evaluated to assess the overall impact on tropical

476   cyclone forecasts.

477

32
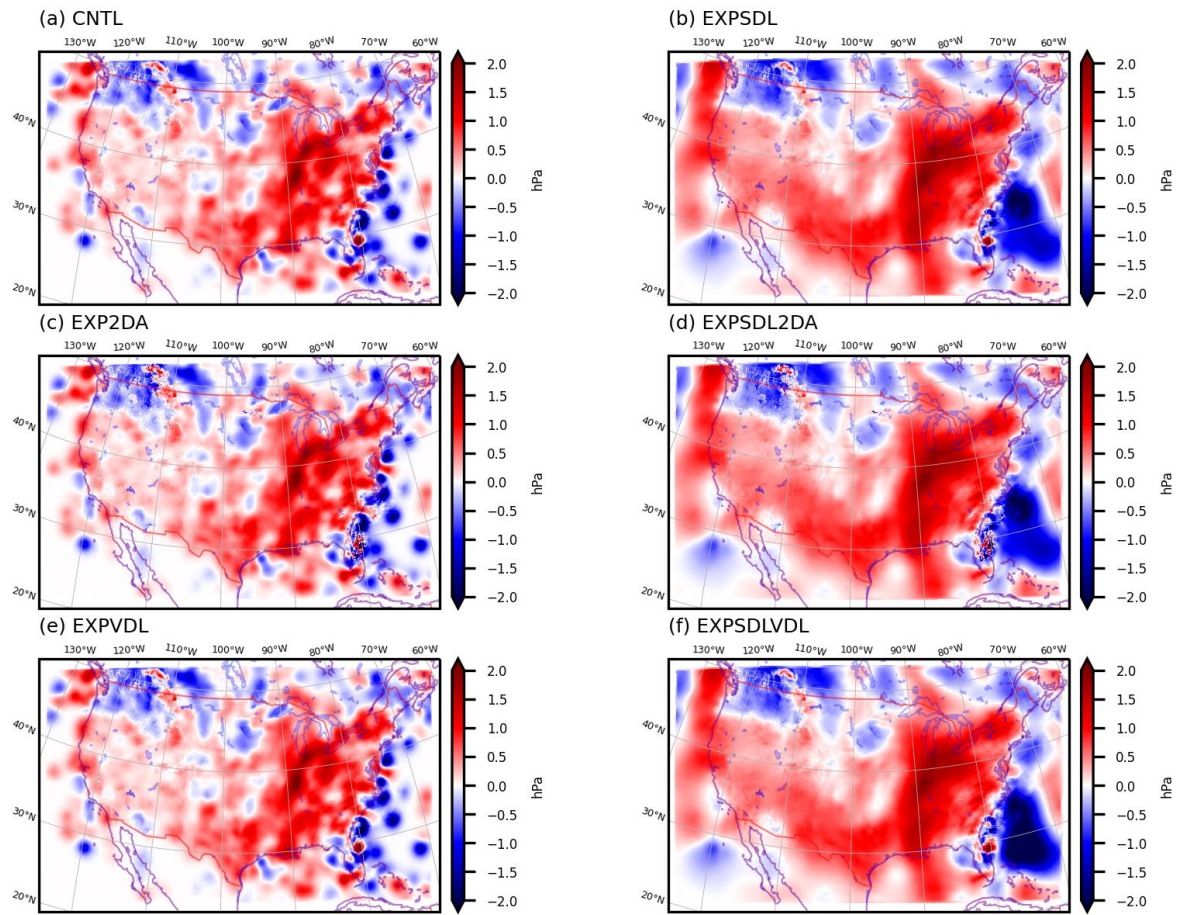
Fig. 11. Analysis increment of surface pressure (hPa) at 16UTC, September 29, 2022, in each experiment (a: CNTL; b: EXPSDL; c: EXP2DA; d: EXPSDL2DA; e: EXPVDL; f: EXPSDLVDL).

(a) surface pressure   (b) temperature
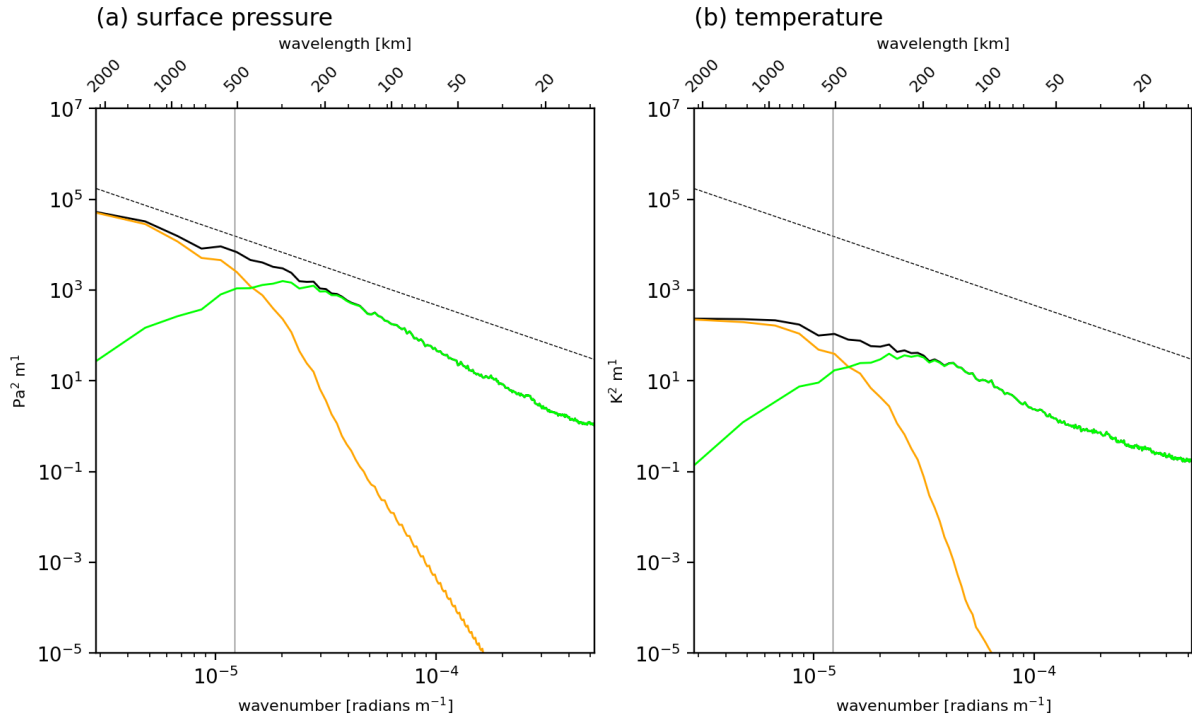
Fig. 12. The power spectra of (a) surface pressure (Pa^2 m) and (b) the lowest-level temperature (K^2 m), in the analysis at 16UTC on September 29, 2022, in EXPSDLVDL (black: original perturbation: orange: filtered perturbation by recursive filter; green: difference between original and filtered perturbations). Gray solid line indicates characteristic wavelength in scale separation (recursive filter $e^{-1/2}$-folding scale). Black dotted line indicates (wavenumber)$^{-5/3}$.
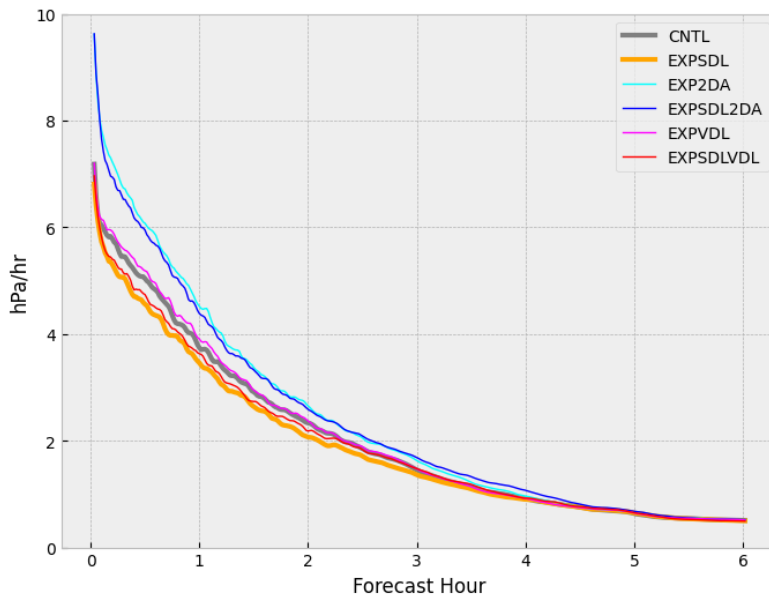
Fig. 13. Mean absolute pressure tendency (hPa hr^{-1}) of the first 6-hour forecasts from the analysis at 00 UTC, September 30, 2022 in each experiment (gray: CNTL; orange: EXPSDL; cyan: EXP2DA; blue: EXPSDL2DA; magenta: EXPVDL; red: EXPSDLVDL).
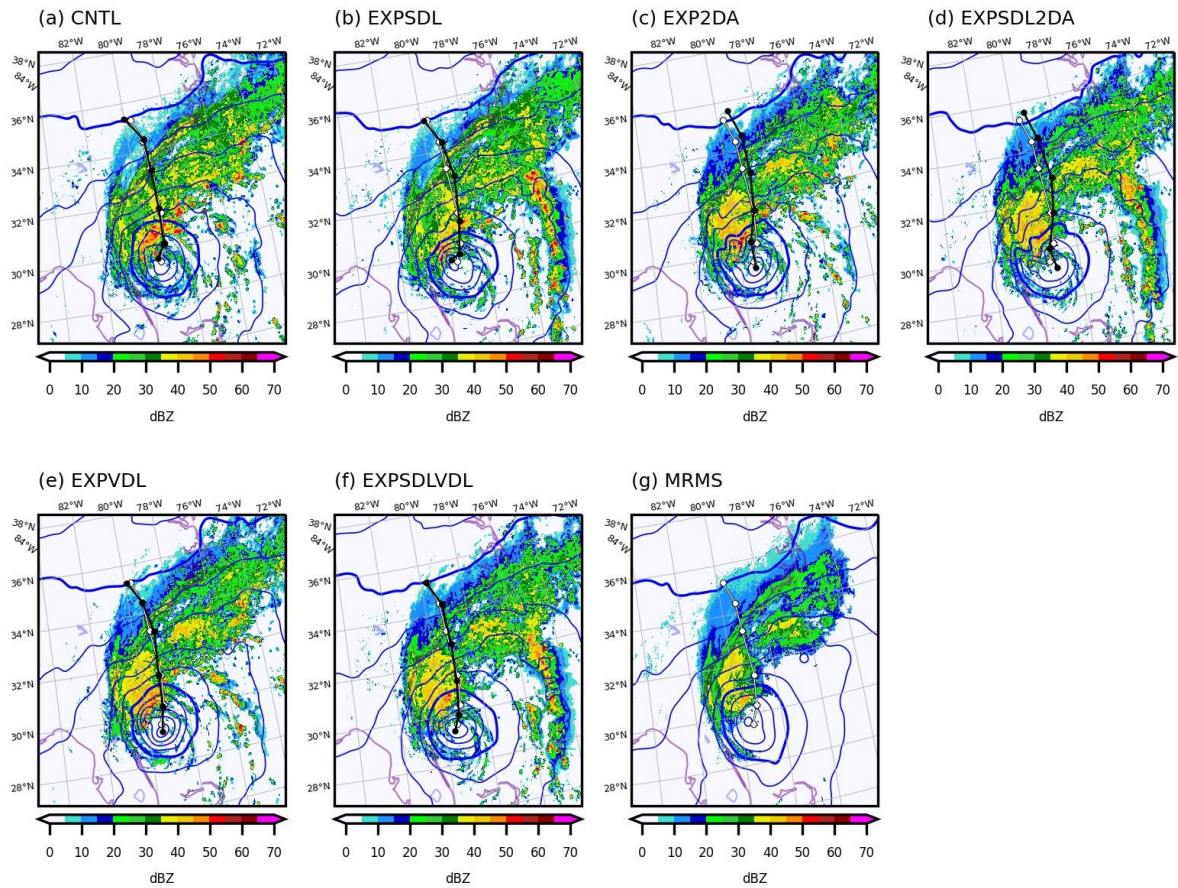
Fig. 14. Composited radar reflectivity (color, dBZ) and SLP (blue contours, every 4 hPa) analyses at 00UTC, September 30, 2022, and Hurricane Ian track forecasts (black lines) in each experiment (a: CNTL; b: EXPSDL; c: EXP2DA; d: EXPSDL2DA; e: EXPVDL; f: EXPSDLVDL) and (g) MRMS observations and HRRR SLP analysis. White lines are Ian's best track.
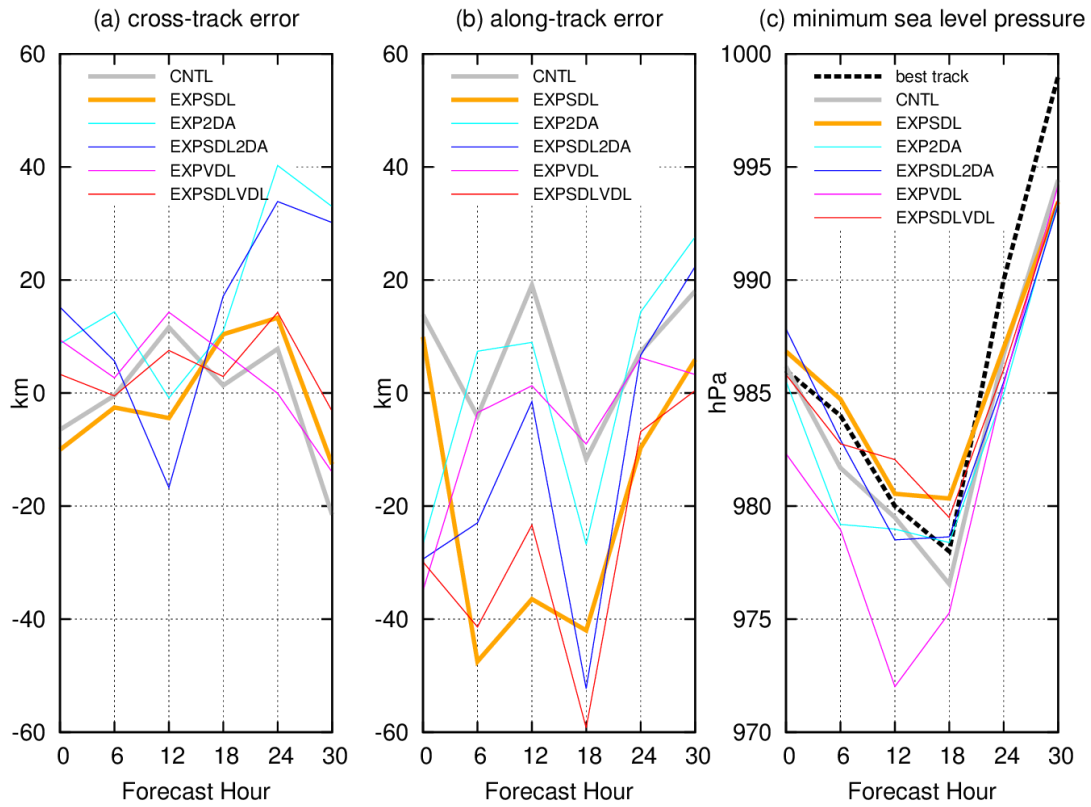
Fig. 15. (a) Cross-track error (positive: right of track) and (b) along-track error (positive: faster) verified against the best track (km) and (c) minimum sea level pressure (hPa) of Hurricane Ian forecasts initialized at 00UTC, September 30, 2022, in each experiment (gray: CNTL; orange: EXPSDL; cyan: EXP2DA; blue: EXPSDL2DA; magenta: EXPVDL; red: EXPSDLVDL). Black dotted line in (c) indicates the best track.

5. Conclusions

In this study, both scale- and variable-dependent localization (SDL and VDL) were implemented in a prototype RRFS. Through sensitivity tests we have shown several advantages of adopting SDL and VDL techniques for convective-scale DA based upon a week-long cycling test and a brief case study with Hurricane Ian.

The advantage of SDL is that the localization radius can be larger while keeping the effect of the sampling error small. It made the analysis increments smoother and was effective in improving the bias of the forecast of low-level temperature and relative humidity (Figs. 6–8) and at decreasing the dynamical imbalance of the analysis (Fig. 13). Although the smoother analysis increment does not necessarily decrease the RMSE of the short-term forecast, it may improve the long-term forecast. In particular, low-level temperature and precipitation were improved for 12-hour forecasts (Figs. 6–8).

On the other hand, the main advantage of VDL is to make the simultaneous conventional and radar reflectivity DA possible. In the conventional localization, the localization radii for all variables including hydrometeors cannot be optimized simultaneously. However, 2DA generated a large imbalance due to too small localization radius for atmospheric variables in radar reflectivity DA (Fig. 13). In assimilating radar reflectivity by VDL, the imbalance became smaller than 2DA (Fig. 13) because of the larger localization radius and the smaller analysis increment of atmospheric variables (Fig. 3b). This imbalance reduction is not achieved only by

37

528   SDL (Appendix C).

529   In both SDL and VDL, the imbalance reduction is important in considering

530   implementation of them in the operational DA system. These methods are beneficial especially

531   in the following situations: (i) the ensemble size is limited, (ii) the imbalance of the analysis

532   largely affects the targeted forecast, and (iii) dense hydrometeor observations are assimilated

533   simultaneously with the other sparse atmospheric observations. In operational regional DA

534   systems, these limitations generally should be considered to assimilate many observations in a

535   tight time limit.

536   SDL and VDL increase the memory usage and the computation time for the localization.

537   However, the computational cost in VDL is smaller than that in 2DA since the number of times

538   of inputting files required to run EnVar (once) is less than that required in 2DA (twice). In this

539   study, the total computation time for EnVar was comparable between EXP2DA and

540   EXPSDLVDL.

541   Since the weight of each scale in SDL is automatically determined depending on the power

542   spectra of the variables, the sensitivity of the localization radius to the forecast is less than the

543   case without SDL (not shown). However, tuning localization radii are still required even with

544   SDL, and the optimal radii depend on variables, vertical levels, seasons, and so on (cf, Appendix

545   C). Adapting different localization radii separately for these components with techniques such

546   as VDL may optimize the localization radii more strictly. However, it makes tuning them more

547 complicated. To prevent manual tuning, new techniques such as the adaptive localization (e.g.,

548 Menetrier and Auligne 2015) should be developed also for SDL and VDL.

Data Availability Statement

Observation data used in this study are openly available at the NOAA Rapid Refresh (RAP) data registry of open data on AWS (https://registry.opendata.aws/noaa-rap/). The DA and forecast system, including the GSI and FV3LAM, used in this study can be obtained from https://github.com/shoyokota/ufs-srweather-app/commits/feature/RRFS_dev1_SDL_VDL.

APPENDIX A

Characteristic wavelength in scale separation with the recursive filter in SDL

The recursive filter $\mathbf{F}_{s,v}$ used for scale separation in Eq. (8) is working as a low-pass filter and the resulting power spectra of ensemble perturbations are quasi-Gaussian in wave space. This characteristic of scale separation is explained as follows.

Since the recursive filter is regarded as a quasi-Gaussian filter (Purser et al. 2003), the filtering kernel of $\mathbf{F}_{s,v}$ in the x-direction is approximated as Gaussian

$$F_\sigma(x) = \frac{1}{\sqrt{2\pi}\sigma} e^{-\frac{x^2}{2\sigma^2}}, \tag{A1}$$

where σ is the $e^{-1/2}$-folding length of the recursive filter and $\int_{-\infty}^{\infty} F_\sigma(x) dx = 1$. Using this Eq. (A1), Fourier response of this $F_\sigma(x)$ is obtained as

$$G_\sigma(k) \equiv \int_{-\infty}^{\infty} F_\sigma(x) e^{-ikx} dx = e^{-\frac{k^2\sigma^2}{2}} \int_{-\infty}^{\infty} \frac{1}{\sqrt{2\pi}\sigma} e^{-\frac{(x+ik\sigma^2)^2}{2\sigma^2}} dx = e^{-\frac{k^2\sigma^2}{2}}. \tag{A2}$$

Eq. (A2) indicates that $G_\sigma(k)$ is also Gaussian in wave space and its characteristic wavenumber k_c defined by $G_\sigma(k_c) \equiv e^{-1/2}$ is $k_c = 1/\sigma$. As a result, the characteristic wavelength of $G_\sigma(k)$ is $\lambda_c \equiv 2\pi/k_c = 2\pi\sigma$. Since the power spectrum density ratio of filtered ensemble perturbations (e.g., Fig. 2) is proportional to $G_\sigma(k)^2$, the ratio is about e^{-1} in wavenumber of $\lambda_c = 2\pi\sigma$ and square roots of power spectrum density ratios of all separated scales sum to one in SDL.

APPENDIX B

Localization of cross-variable covariance in VDL

In EXPVDL and EXPSDLVDL, the parameter making the cross-variable correlation smaller was applied to mitigate overestimation of analysis increments. This overestimation is caused by the horizontally-integrated localization function in VDL, which is larger than that applied for radar reflectivity in general. Details are explained as follows.

When the filtering kernels of $\mathbf{L}_{s,v}$ and $\mathbf{L}_{s,v}^{1/2}$ in x-direction are written as $L_\sigma(x)$ and $C_\sigma(x)$, respectively, their relationship should be written as:

$$L_\sigma(x) = \int_{-\infty}^{\infty} C_\sigma(x - x')C_\sigma(x')dx' = e^{-\frac{x^2}{2\sigma^2}}. \tag{B1}$$

Note that the normalization factor is different between $L_\sigma(x)$ in Eq. (B1) and $F_\sigma(x)$ in Eq. (A1) because the peak value of $\mathbf{L}_{s,v}$ should be one. From this Eq. (B1), $C_\sigma(x)$ is obtained as:

$$C_\sigma(x) = \left(\frac{2}{\pi\sigma^2}\right)^{1/4} e^{-\frac{x^2}{\sigma^2}}. \tag{B2}$$

Using this Eq. (B2), the localization applied for cross-variable covariances in VDL is based on the following kernel:

$$L_{\sigma_1,\sigma_2}(x) = \int_{-\infty}^{\infty} C_{\sigma_1}(x - x')C_{\sigma_2}(x')dx' = \sqrt{\frac{2\sigma_1\sigma_2}{\sigma_1^2 + \sigma_2^2}} e^{-\frac{x^2}{\sigma_1^2+\sigma_2^2}}, \tag{B3}$$

where $\sigma_1 \gg \sigma_2$. According to Eq. (B3), the peak value of $L_{\sigma_1,\sigma_2}(x)$ is less than one, and the ratio of horizontally-integrated $L_{\sigma_1,\sigma_2}(x)L_{\sigma_1,\sigma_2}(y)$ and $L_{\sigma_2}(x)L_{\sigma_2}(y)$ is calculated as:

$$\frac{\int_{-\infty}^{\infty} L_{\sigma_1,\sigma_2}(x)L_{\sigma_1,\sigma_2}(y)dxdy}{\int_{-\infty}^{\infty} L_{\sigma_2}(x)L_{\sigma_2}(y)dxdy} = \frac{\sigma_1}{\sigma_2} \gg 1. \tag{B4}$$

594　　Eq. (B4) means that the total assimilation effect of the variables localized by $L_{\sigma_1,\sigma_2}(x)L_{\sigma_1,\sigma_2}(y)$

595　　in VDL is σ_1/σ_2 times as large as that by $L_{\sigma_2}(x)L_{\sigma_2}(y)$ in the single-scale localization. The

596　　larger assimilation effect does not necessarily make the analysis increment larger in case the

597　　effects of multiple observations are canceled by each other. However, they are not canceled in

598　　case the first guess departure of radar reflectivity has large bias. To mitigate this overestimation

599　　of the analysis increment in this case, multiplying the factor $(\leq \sigma_2/\sigma_1)$ to $L_{\sigma_1,\sigma_2}(x)L_{\sigma_1,\sigma_2}(y)$

600　　is effective. The solid gray, dashed gray, and magenta lines in Fig. 3b indicates the distributions

601　　of $L_{\sigma_1}(x)L_{\sigma_1}(y)$, $L_{\sigma_2}(x)L_{\sigma_2}(y)$, and $(\sigma_2/\sigma_1)L_{\sigma_1,\sigma_2}(x)L_{\sigma_1,\sigma_2}(y)$, respectively, against $r =$

602　　$\sqrt{x^2 + y^2}$ in the case of $\sigma_2/\sigma_1 = 15/300 = 0.05$. Without multiplying this factor in

603　　EXPVDL the first guess departure became larger because the impact of assimilated radar

604　　reflectivity became too large (not shown).

605

43

APPENDIX C

Additional sensitivity experiments to support the necessity of SDL and VDL

To support the advantage of SDL compared to SSL with a larger localization length, the same experiment as CNTL except with larger horizontal localization length (EXPSSL1200, $e^{-20/3}$-folding scale: 1200 km) was conducted from 15 UTC, September 29 to 00 UTC, September 30, 2022. In addition, the same experiment as EXPSDLVDL except with 3-scale SDL instead of VDL (EXPSDL3, $e^{-20/3}$-folding localization lengths: 1200, 300, and 15 km) was also conducted in the same period to support the advantage of VDL compared to SDL with smaller localization length for the smallest scale. In EXPSDL3, the first and second scales were separated in the same way as EXPSDLVDL. The second and third scales were separated by the horizontal recursive filter with 15-km $e^{-20/3}$-folding scales. Each localization length was applied for all variables.

In EXPSSL1200, the RMSE of the first guess departure was significantly worse than those in both CNTL and EXPSDL (Figs. A1a–c) although the bias was almost the same as that in EXPSDL (Figs. A1d–f). It indicates that too large localization lengths disturb the analysis by sampling error and SDL is necessary to enlarge the localization length.

In EXPSDL3, both of the RMSE and the bias of the first guess departure were significantly worse than those in EXPSDLVDL (Figs. A1a–f). Furthermore, mean absolute pressure

44

625   tendency in EXPSDL3 was over 3 times larger than that in EXPSDLVDL (not shown). These

626   indicates the necessity of VDL in association with dense radar reflectivity observations. Namely,

627   to avoid introducing large imbalance localization lengths for hydrometeor variables should be

628   short, even for the large-scale ensemble covariances.

629
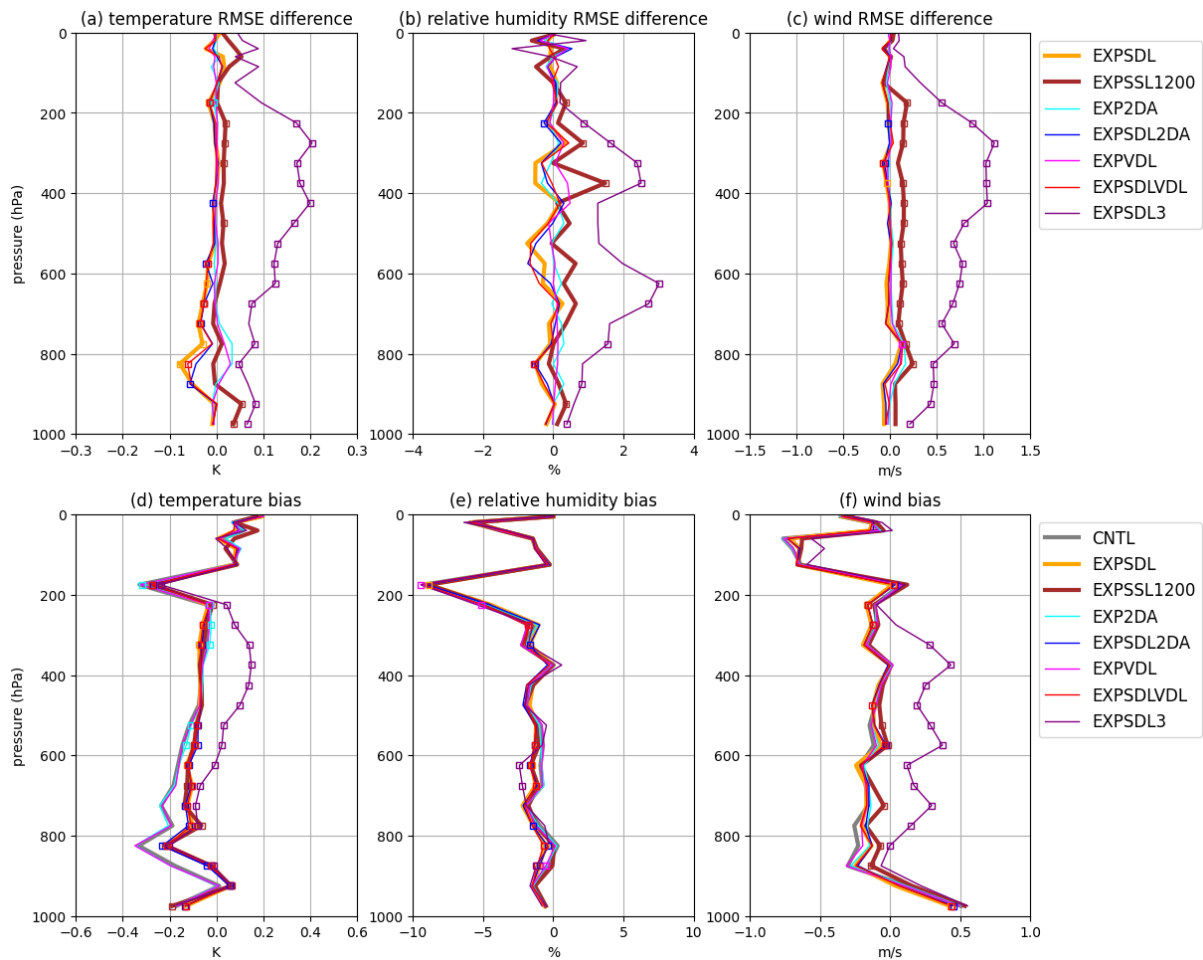
Fig. A1. Same as Fig. 6 but in each cycling experiment from 15 UTC, September 29 to 00 UTC, September 30, 2022 (gray: CNTL; orange: EXPSDL; brown: EXPSSL1200; cyan: EXP2DA; blue: EXPSDL2DA; magenta: EXPVDL; red: EXPSDLVDL; purple: EXPSDL3).

REFERENCES

Angevine, W. M., Olson, J., Gristey, J. J., Glenn, I., Feingold, G., & Turner, D. D. (2020). Scale Awareness, Resolved Circulations, and Practical Limits in the MYNN-EDMF Boundary Layer and Shallow Cumulus Scheme. *Monthly Weather Review*, **148**(11), 4629–4639. https://doi.org/10.1175/mwr-d-20-0066.1

Beljaars, A. C. M., Brown, A. R., & Wood, N. (2004). A new parametrization of turbulent orographic form drag. *Quarterly Journal of the Royal Meteorological Society*, **130**(599), 1327–1347. https://doi.org/10.1256/qj.03.73

Benjamin, S. G., Devenyi, D., Weygandt, S. S., Brundage, K. J., Brown, J. M., Grell, G. A., Kim, D, Schwartz, B. E., Smirnova, T. G., Smith, T. L., & Manikin, G. S. (2004). An hourly assimilation–forecast cycle: The RUC. *Monthly Weather Review*, **132**(2), 495–518, https://doi.org/10.1175/1520-0493(2004)132<0495:AHACTR>2.0.CO;2

Benjamin, S. G., Weygandt, S. S., Brown, J. M., Hu, M., Alexander, C. R., Smirnova, T. G., Olson, J. B., James, E. P., Dowell, D. C., Grell, G. A., Lin, H., Peckham, S. E., Smith, T. L., Moninger, W. R., Kenyon, J. S., & Manikin, G. S. (2016). A North American hourly assimilation and model forecast cycle: The Rapid Refresh. *Monthly Weather Review*, **144**(4), 1669–1694, https://doi.org/10.1175/MWR-D-15-0242.1

Benjamin, S. G., Smirnova, T. G., James, E. P., Lin, L.-F., Hu, M., Turner, D. D., & He, S. (2022). Land-snow data assimilation including a moderately coupled initialization

654   method applied to NWP. *Journal of Hydrometeorology*, **23**(6), 825–845.

655   https://doi.org/10.1175/JHM-D-21-0198.1

656 Benjamin, S. G., James, E. P., Hu, M., Alexander, C. R., Ladwig, T. T., Brown, J. M.,

657   Weygandt, S. S., Turner, D. D., Minnis, P., Smith, W. L., & Heidinger, A. K. (2021).

658   Stratiform Cloud-Hydrometeor Assimilation for HRRR and RAP Model Short-Range

659   Weather Prediction. *Monthly Weather Review*, **149**(8), 2673–2694.

660   https://doi.org/10.1175/MWR-D-20-0319.1

661 Black, T. L., & Coauthors (2021). A Limited Area Modeling Capability for the Finite-Volume

662   Cubed-Sphere (FV3) Dynamical Core and Comparison With a Global Two-Way Nest.

663   *Journal of Advances in Modeling Earth Systems*, **13**(6), e2021MS002483.

664   https://doi.org/10.1029/2021MS002483

665 Bucci, L., Alaka, L., Hagen, A., Delgado, S., & Beven, J. (2023). Hurricane Ian (AL092022).

666   *National Hurricane Center Tropical Cyclone Report*, 72pp,

667   https://www.nhc.noaa.gov/data/tcr/AL092022_Ian.pdf

668 Buehner, M. (2012). Evaluation of a spatial/spectral covariance localization approach for

669   atmospheric data assimilation. *Monthly Weather Review*, **140**(2), 617–636.

670   https://doi.org/10.1175/MWR-D-10-05052.1

671 Buehner, M., & Shlyaeva, A. (2015). Scale-dependent background-error covariance

672   localisation. *Tellus A*, **67**(1), 28027, https://doi.org/10.3402/tellusa.v67.28027

48

673   Carley, J. R., Pyle, M. E., Alexander, C. R., & Weygandt, S. (2023). On the Development of

674   NOAA's Rapid Refresh Forecast System. *Working Group on Numerical*

675   *Experimentation Research Activity in Earth System Modelling*, **53**, 5.07–5.08.

676   https://wgne.net/bluebook/uploads/2023/docs/05_Carley_Jacob_RapidRefreshModel.pdf

677   Caron, J.-F., & Buehner, M. (2018). Scale-dependent background error covariance

678   localization: Evaluation in a global deterministic weather forecasting system. *Monthly*

679   *Weather Review*, **146**(5), 1367–1381. https://doi.org/10.1175/MWR-D-17-0369.1

680   Caron, J.-F., & Buehner, M. (2022). Implementation of scale-dependent background-error

681   covariance localization in the Canadian global deterministic prediction system. *Weather*

682   *and Forecasting*, **37**(9), 1567–1580. https://doi.org/10.1175/WAF-D-22-0055.1

683   Caron, J.-F., Michel, Y., Montmerle, T., & Arbogast, E. (2019). Improving background error

684   covariances in a 3D ensemble-variational data assimilation system for regional NWP.

685   *Monthly Weather Review*, **147**(1), 135–151. https://doi.org/10.1175/MWR-D-18-0248.1

686   Crum, T. D., & Alberty, R. L. (1993). The WSR-88D and the WSR-88D operational support

687   facility. *Bulletin of the American Meteorological Society*, **74**(9), 1669–1688.

688   https://doi.org/10.1175/1520-0477(1993)074<1669:TWATWO>2.0.CO;2

689   Dong, J. & Xue, M. (2013). Assimilation of radial velocity and reflectivity data from coastal

690   WSR-88D radars using an ensemble Kalman filter for the analysis and forecast of

landfalling hurricane Ike (2008). *Quarterly Journal of the Royal Meteorological Society*, **139**(671), 467–487. https://doi.org/10.1002/qj.1970

Dowell, D. C., & Coauthors (2022). The High-Resolution Rapid Refresh (HRRR): An hourly updating convection-allowing forecast model. Part I: Motivation and system description. *Weather and Forecasting*, **37**(8), 1371–1395. https://doi.org/10.1175/WAF-D-21-0151.1

Evensen, G. (1994). Sequential data assimilation with a nonlinear quasi-geostrophic model using Monte Carlo methods to forecast error statistics. *Journal of Geophysical Research*, **99**(C5), 10143–10162. https://doi.org/10.1029/94JC00572

Gaspari, G., & Cohn, S. E. (1999). Construction of correlation functions in two and three dimensions. *Quarterly Journal of the Royal Meteorological Society*, **125**(554), 723–757. https://doi.org/10.1002/qj.49712555417

Greybush, S. J., Kalnay, E., Miyoshi, T., Ide, K., & Hunt, B. R. (2011). Balance and Ensemble Kalman Filter Localization Techniques. *Monthly Weather Review*, **139**(2), 511–522. https://doi.org/10.1175/2010MWR3328.1

Hamill, T. M., & Snyder, C. (2000). A hybrid ensemble Kalman filter-3D variational analysis scheme. *Monthly Weather Review*, **128**(8), 2905–2919. https://doi.org/10.1175/1520-0493(2000)128<2905:AHEKFV>2.0.CO;2

Hamill, T. M., Whitaker, J. S. & Snyder, C. (2001). Distance-dependent filtering of background error covariance estimates in an ensemble Kalman filter. *Monthly Weather*

Review, **129**(11), 2776–2790. https://doi.org/10.1175/1520-

0493(2001)129<2776:DDFOBE>2.0.CO;2

Houtekamer, P. L., & Mitchell, H. L. (2001). A sequential ensemble Kalman filter for

atmospheric data assimilation. *Monthly Weather Review*, **129**(1), 123–137.

https://doi.org/10.1175/1520-0493(2001)129<0123:ASEKFF>2.0.CO;2

Huang, B., Wang, X., Kleist, D. T., & Lei, T. (2021). A simultaneous multiscale data

assimilation using scale-dependent localization in GSI-based hybrid 4DEnVar for NCEP

FV3-based GFS. *Monthly Weather Review*, **149**(2), 479–501.

https://doi.org/10.1175/MWR-D-20-0166.1

Hunt, B. R., Kostelich, E. J., & Szunyogh, I. (2007). Efficient data assimilation for

spatiotemporal chaos: A local ensemble transform Kalman filter. *Physica D*, **230**(1–2),

112–126. https://doi.org/10.1016/j.physd.2006.11.008

Iacono, M. J., Delamere, J. S., Mlawer, E. J., Shephard, M. W., Clough, S. A., & Collins, W.

D. (2008). Radiative forcing by long-lived greenhouse gases: Calculations with the AER

radiative transfer models. *Journal of Geophysical Research*, **113**(D13). D13103.

https://doi.org/10.1029/2008JD009944

Janjic, Z. I. (2003). A nonhydrostatic model based on a new approach. *Meteorology and*

Atmospheric Physics, **82**, 271–285. https://doi.org/10.1007/s00703-001-0587-6

728   Janjic, Z. I., & Gall, R. L. (2012). Scientific documentation of the NCEP nonhydrostatic

729   multiscale model on the B grid (NMMB). Part 1: Dynamics (No. NCAR/TN-489+STR).

730   University Corporation for Atmospheric Research, 75 pp.

731   https://doi.org/10.5065/D6WH2MZX

732   Johnson, A. & Wang, X. (2017). Design and implementation of a GSI-based convection-

733   allowing ensemble data assimilation and forecast system for the PECAN field

734   experiment. Part I: optimal configurations for nocturnal convection prediction using

735   retrospective cases. *Weather and Forecasting*, **32**(1), 289–315.

736   https://doi.org/10.1175/WAF-D-16-0102.1

737   Lei, L., Whitaker, J. S., & Bishop, C. (2018). Improving assimilation of radiance observations

738   by implementing model space localization in an ensemble Kalman filter. *Journal of*

739   *Advances in Modeling Earth Systems*, **10**(12), 3221–3232.

740   https://doi.org/10.1029/2018MS001468

741   Lin, S.-J. (2004). A "vertically lagrangian" finite-volume dynamical core for global models.

742   *Monthly Weather Review*, **132**(10), 2293–2307. https://doi.org/10.1175/1520-

743   0493(2004)132<2293:AVLFDC>2.0.CO;2

744   Liu, S., DiMego, G., Guan, S., Kumar, V. K., Keyser, D., Xu, Q., Nai, K., Zhang, P., Liu, L.,

745   Zhang, J., Howard, L., & Ator, J. (2016). WSR-88D Radar Data Processing at NCEP.

746   *Weather and Forecasting*, **31**(6), 2047–2055. https://doi.org/10.1175/WAF-D-16-0003.1

Lorenc, A. C. (2003). The potential of the ensemble Kalman filter for NWP: a comparison

with 4D-Var. *Quarterly Journal of the Royal Meteorological Society*, **129**(595), 3183–

3203. https://doi.org/10.1256/qj.02.132

Menetrier, B., & Auligne, T. (2015): Optimized localization and hybridization to filter

ensemble-based covariances. *Monthly Weather Review*, **143**(10), 3931–3947.

https://doi.org/10.1175/MWR-D-15-0057.1

Michel, Y., Auligne, T., & Montmerle, T. (2011). Heterogeneous convective-scale

background error covariances with the inclusion of hydrometeor variables. *Monthly

Weather Review*, **139**(9), 2994–3015. https://doi.org/10.1175/2011MWR3632.1

Miyoshi, T., & Kondo, K. (2013). A multi-scale localization approach to an ensemble Kalman

filter. *SOLA*, **9**, 170–173. https://doi.org/10.2151/sola.2013-038

Mlawer, E. J., Taubman, S. J., Brown, P. D., Iacono, M. J., & Clough, S. A. (1997). Radiative

transfer for inhomogeneous atmospheres: RRTM, a validated correlated-k model for the

longwave. *Journal of Geophysical Research*, **102**(D14), 16663–16682.

https://doi.org/10.1029/97JD00237

Nakanishi, M., & Niino, H. (2009). Development of an improved turbulence closure model

for the atmospheric boundary layer. *Journal of the Meteorological Society of Japan*,

87(5), 895–912. http://doi.org/10.2151/jmsj.87.895

765   NCEI (2023). NOAA Storm Events Database. Accessed July 2023,

766   https://www.ncdc.noaa.gov/stormevents/

767   Olson, J. B., Kenyon, J. S., Angevine, W. A., Brown, J. M., Pagowski, M., & Suselj, K.

768   (2019). A Description of the MYNN-EDMF Scheme and the Coupling to Other

769   Components in WRF–ARW. *NOAA Technical Memorandum OAR GSD*, **61**.

770   https://doi.org/10.25923/n9wm-be49

771   Olson, J. B., Smirnova, T., Kenyon, J. S., Turner, D. D., Brown, J. M., Zheng, W., & Green,

772   B. W. (2021). A Description of the MYNN Surface-Layer Scheme. *NOAA Technical*

773   *Memorandum OAR GSL*, **67**. https://doi.org/10.25923/f6a8-bc75

774   Perianez, A., Reich, H., & Potthast, R. (2014). Optimal localization for ensemble Kalman

775   filter systems. *Journal of the Meteorological Society of Japan*, **92**(6), 585–597.

776   https://doi.org/10.2151/jmsj.2014-605

777   Purser, R. J., Wu, W. S., Parrish, D. F., & Roberts, N. M. (2003). Numerical aspects of the

778   application of recursive filters to variational statistical analysis. Part I: Spatially

779   homogeneous and isotropic Gaussian covariances. *Monthly Weather Review*, **131**(8),

780   1524–1535. https://doi.org/10.1175//1520-0493(2003)131<1524:NAOTAO>2.0.CO;2

781   Putman, W. M., & Lin, S.-J. (2007). Finite-volume transport on various cubed-sphere grids.

782   *Journal of Computational Physics*, **227**(1), 55–78.

783   https://doi.org/10.1016/j.jcp.2007.07.022

Roberts, B., Jirak, I. L., Clark, A. J., Weiss, S. J., & Kain, J. S. (2019). Postprocessing and

visualization techniques for convection-allowing ensembles. *Bulletin of the American

Meteorological Society*, **100**(7), 1245–1258. https://doi.org/10.1175/BAMS-D-18-0041.1

Roberts, B., Gallo, B. T., Jirak, I. L., Clark, A. J., Dowell, D. C., Wang, X., & Wang, Y.

(2020). What does a convection-allowing ensemble of opportunity buy us in forecasting

thunderstorms? *Weather and Forecasting*, **35**(6), 2293–2316.

https://doi.org/10.1175/WAF-D-20-0069.1

Smirnova, T. G., Brown, J. M., & Benjamin, S. G. (1997). Performance of different soil

model configurations in simulating ground surface temperature and surface fluxes.

Monthly Weather Review, **125**(8), 1870–1884. https://doi.org/10.1175/1520-

0493(1997)125<1870:PODSMC>2.0.CO;2

Smirnova, T. G., Brown, J. M., Benjamin, S. G. & Kim, D. (2000). Parameterization of cold-

season processes in the MAPS land-surface scheme. *Journal of Geophysical Research*,

105(D3), 4077–4086. https://doi.org/10.1029/1999JD901047

Smirnova, T. G., Brown, J. M., Benjamin, S. G., & Kenyon, J. S. (2016). Modifications to the

Rapid Update Cycle land surface model (RUC LSM) available in the weather Research

and forecasting model. *Monthly Weather Review*, **144**(5), 1851–1865.

https://doi.org/10.1175/MWR-D-15-0198.1

Smith, T. M., & Coauthors (2016). Multi-Radar Multi-Sensor (MRMS) severe weather and

aviation products: Initial operating capabilities. *Bulletin of the American Meteorological Society*, **97**(9), 1617–1630. https://doi.org/10.1175/BAMS-D-14-00173.1

Thompson, G., & Eidhammer, T. (2014). A Study of Aerosol Impacts on Clouds and

Precipitation Development in a Large Winter Cyclone. *Journal of the Atmospheric Sciences*, **71**(10), 3636–3658. https://doi.org/10.1175/jas-d-13-0305.1

Tsiringakis, A., Steeneveld, G. J., & Holtslag, A. A. M. (2017). Small-scale orographic

gravity wave drag in stable boundary layers and its impact on synoptic systems and near-surface meteorology. *Quarterly Journal of the Royal Meteorological Society*, **143**(704), 1504–1516. https://doi.org/10.1002/qj.3021

Wang, X., Parrish, D., Kleist, D., & Whitaker, J. (2013). GSI 3DVar-based ensemble–

variational hybrid data assimilation for NCEP global forecast system: Single-resolution experiments. *Monthly Weather Review*, **141**(11), 4098–4117.

https://doi.org/10.1175/MWR-D-12-00141.1

Wang, Y., & Wang, X. (2017). Direct assimilation of radar reflectivity without tangent linear

and adjoint of the nonlinear observation operator in the GSI-based EnVar system:

Methodology and experiment with the 8 May 2003 Oklahoma City tornadic supercell.

Monthly Weather Review, **145**(4), 1447–1471. https://doi.org/10.1175/MWR-D-16-0231.1

821 Wang, Y., & Wang, X. (2023). Simultaneous multiscale data assimilation using scale- and

822 variable-dependent localization in EnVar for convection allowing analyses and forecasts:

823 Methodology and experiments for a tornadic supercell. *Journal of Advances in Modeling*

824 *Earth Systems*, **15**(5), e2022MS003430. https://doi.org/10.1029/2022MS003430

825 Wang, Y., & Wang, X. (2024). Improving CONUS convective-scale forecasting with

826 simultaneous multiscale data assimilation: A squall line case study. *Journal of*

827 *Geographical Research: Atmospheres*, in review.

828 Wang, X., Chipilski, H. G., Bishop, C. H., Satterfield, E., Baker, N., & Whitaker, J. S. (2021).

829 A multiscale local gain form ensemble transform Kalman filter (MLGETKF). *Monthly*

830 *Weather Review*, **149**(3), 605–622. https://doi.org/10.1175/MWR-D-20-0290.1

831 Whitaker, J. S., & Hamill, T. M. (2002). Ensemble data assimilation without perturbed

832 observations. *Monthly Weather Review*, **130**(7), 1913–1924.

833 https://doi.org/10.1175/1520-0493(2002)130<1913:EDAWPO>2.0.CO;2

834 Whitaker, J. S., & Hamill, T. M. (2012). Evaluating methods to account for system errors in

835 ensemble data assimilation. *Monthly Weather Review*, **140**(9), 3078–3089.

836 https://doi.org/10.1175/MWR-D-11-00276.1

837 Zhang, F., Weng, Y., Sippel, J. A., Meng, Z., & Bishop, C. H. (2009). Cloud-resolving

838 hurricane initialization and prediction through assimilation of Doppler radar observations

with an ensemble Kalman filter. *Monthly Weather Review*, **137**(7), 2105–2125.

https://doi.org/10.1175/2009MWR2645.1